Geotextiles and Geomembranes 37 (2013) 81–98

Contents lists available at SciVerse ScienceDirect

Geotextiles and Geomembranes

journal homepage: www.elsevier.com/locate/geotexmem

Behavior of sandy slopes remediated by EPS-block geofoam under seepage flow

Onur Akay [a,*], A. Tolga Özer [a], Garey A. Fox [b], Steven F. Bartlett [c], David Arellano [d]

[a] Department of Civil Engineering, Okan University, Tuzla Campus, Istanbul 34959, Turkey
[b] Department of Biosystems and Agricultural Engineering, Oklahoma State University, 120 Ag Hall Stillwater, OK 74078-6016, USA
[c] Department of Civil and Environmental Engineering, University of Utah, 110 Central Campus Dr., Salt Lake City, UT 84112, USA
[d] Department of Civil Engineering, The University of Memphis, 104 Engineering Science Building, Memphis, TN 38152-3180, USA

ARTICLE INFO

Article history:
Received 8 October 2012
Received in revised form
14 February 2013
Accepted 16 February 2013
Available online

Keywords:
EPS-block geofoam
Slope stability
Seepage

ABSTRACT

Expanded polystyrene (EPS) geofoam (geofoam block) is commonly used as a lightweight fill for many civil engineering applications. However, when used for slope remediation, the behavior of geofoam block for slope systems undergoing seepage flow is not well known. In this study, a total of 36 laboratory lysimeter experiments (dimensions of 60 cm height, 20 cm width, and 200 cm length) were conducted to investigate the behavior of sandy slopes containing geofoam blocks as a lightweight fill material. These experiments were conducted with three different values of constant water pressure in the water reservoir located at one end of the lysimeter. In addition, three different configurations of geofoam block were tested with geofoam blocks placed on the face of the packed sandy slope. The dimensions of the geofoam blocks were 2.5 cm high, 5 cm wide, and 15 cm long to achieve a 1:20 scale corresponding to actual block size that is commonly manufactured. Laboratory physical test results were quantified by coupled seepage flow and slope stability models showing the adverse effect of seepage on the factor of safety (FS). Geofoam block configurations were found to be stable against seepage conditions which would cause a shallow-seated failure of the slope in the absence of the geofoam blocks. This is due to the fact that the geofoam blocks could completely fill the mass of the existing slope material subjected to failure. However, the geofoam block configurations were unstable against seepage conditions that resulted in deep-seated failures of marginally stable, sand slopes.

1. Introduction

Expanded polystyrene (EPS) geofoam (geofoam block) is a lightweight, closed, cellular, geosynthetic material which is used for many civil engineering applications, e.g., compressible inclusions (Negussey and Sun, 1996; Horvath, 1997), seismic buffers (Bathurst et al., 2007; Zarnani and Bathurst, 2007), lightweight embankment fills (Beinbrech and Hillmann, 1997; Bartlett et al., 2000, 2001; Aabøe, 2011), railway embankments (O'Brien, 2001), settlement mitigations (Farnsworth et al., 2008), ground vibration isolations (Murillo et al., 2009), and pipeline protections against earthquakes (Lingwall, 2011; Bartlett et al., 2011). The strength and dynamic properties of geofoam blocks have been extensively investigated in previous research (Duskov, 1997; Elragi, 2000; Trandafir et al., 2010; Ossa and Romo, 2010), and recommended design guidelines for highway embankments have been provided by Stark et al. (2004a, b).

Nonetheless, slope stability has been one of the major challenges for geotechnical engineers. Seepage and piping are the common causes of reported slope failures for embankments, levees, earth dams, hillslopes, and streambanks (Fox and Wilson, 2010). Remediation of such failures costs billions of dollars per year (e.g., construction of retaining walls, soil-nail walls, land acquisitions for the right-of-ways to flatten the slopes, etc.). Reducing the driving force of the potential slide is a viable and economical option for increasing the factor of safety of slopes. For this reason, several lightweight fill materials such as tyre bales (Prikryl et al., 2005), shredded tires (Read et al., 1991), wood chips (Coulter, 1975; Kilian, 1984), pumice (Sharma and Buu, 1992), and geofoam blocks (Yeh and Gilmore, 1989; Jutkofsky, 1998; Jutkofsky et al., 2000; Sheeley, 2000; Reuter and Rutz, 2000; Reuter, 2001; Negussey, 2002; Mann and Stark, 2007) have been successfully used to remediate slopes.

Application of geofoam blocks for slope stabilization was implemented in projects in Japan, largely in the mid-1980s to the

* Corresponding author. Tel.: +90 216 6771630x1974; fax: +90 216 6771486.
E-mail addresses: onur.akay@okan.edu.tr (O. Akay), tolga.ozer@okan.edu.tr (A.T. Özer), garey.fox@okstate.edu (G.A. Fox), bartlett@civil.utah.edu (S.F. Bartlett), darellan@memphis.edu (D. Arellano).

0266-1144/$ – see front matter © 2013 Elsevier Ltd. All rights reserved.
http://dx.doi.org/10.1016/j.geotexmem.2013.02.005

mid-1990s (EDO, 1996). The Japanese design procedure for the use of geofoam blocks for slope stabilization includes many of the steps included in the recommended design guideline for stand-alone EPS-block geofoam embankments over soft soil by Stark et al. (2004a, b). In addition, although Tsukamoto (1996) and Negussey (2002) provided general design guidance for the use of geofoam blocks in slope stability projects, these authors do not provide specific guidelines or procedures.

The National Cooperative Highway Research Program (NCHRP) funded a study to develop design guidelines for use of geofoam blocks for slope stabilization and repair projects (NCHRP Project 24-11(02)). Based on this study, the framework for interim design guidelines (Arellano et al., 2009, 2010) and the recommended design procedures (Arellano et al., 2011a,b) were presented for geofoam block for slope stabilization and repair. In these studies, major components of geofoam block slope systems have been defined and external, internal and pavement system failure modes have been conceptually studied. Complete design procedure algorithms for geofoam block slope fills were presented based on conceptual failure modes.

As a result of NCHRP Project 24-11(02), Arellano et al. (2011a) presented a comprehensive document that provided design guidance to facilitate the use of geofoam blocks for slope stabilization and repair. This design procedure is based on the assumption that the adjacent slope is self-stable; however, supporting structures such as structural facing wall, retaining wall or anchored facing systems can be considered to prevent horizontal sliding of the geofoam blocks due to a non-stable adjacent slope. In addition, this design procedure does not address the presence of hydraulic (i.e., seepage) forces acting on the geofoam blocks. Many of the geofoam slope case histories evaluated in the NCHRP 24-11(02) project included the use of underdrain systems below the geofoam blocks, and in some cases drainage system between the adjacent upper slope material and the geofoam blocks were implemented to collect and divert seepage water and thereby alleviating such forces (Arellano et al., 2011a). Based on this current design philosophy and precedent, the design guidelines recommended that all geofoam block slope systems incorporate permanent drainage systems to prevent water from accumulating above the base of the geofoam blocks (lowest level of geofoam blocks). However with time, groundwater tables may rise due to clogging of drainage systems resulting from improper design and/or maintenance, and this could adversely affect the stability of the slope. Therefore, this situation should be evaluated for the long-term behavior of geofoam block slope systems subjected to seepage flow.

There is an uncertainty about selecting the strength properties of geofoam block for external slope stability analysis (Stark et al., 2004a; Arellano et al., 2011a). Until now, these analyses were not studied using laboratory physical geofoam block slope models. Arellano et al. (2011a) recommended conducting further research using numerical modeling, physical testing, and/or observation of full-scale structures to determine whether or not an external slope stability failure induces failure through individual geofoam blocks, or whether the geofoam blocks remain intact and displace as individual elements as a result of slope instability.

The overall objective of this study is to evaluate the stability of geofoam blocks with seepage forces present. This is accomplished by observing the behavior of geofoam block slope systems under seepage using scaled, laboratory experiments with a marginally stable, adjacent, sand slope. For this purpose, small scale (1:20) laboratory physical slope modeling technique under normal gravity (1-g model test) has been adopted. This method has been successfully performed by various researchers (Leshchinsky and Lambert, 1991; Yoo, 2001; Dash et al., 2003; El Sawwaf, 2007; Latha and Somwanshi, 2009; Choudhary et al., 2010; Kousik et al., 2011). Even though the 1-g small scale laboratory physical model test is a valuable technique, because of the scale effect it may not represent the same behavior of the field prototype (Choudhary et al., 2010) due to the differences in stress levels (El Sawwaf, 2007). Therefore, while the results of this research are relevant to revealing insights of failure mechanisms of sandy slopes remediated by EPS-block geofoam under seepage forces at 1:20 scale, they cannot be directly used for field prototypes. Nonetheless, this research also includes coupled seepage and stability numerical modeling to aid in the selection of the hydraulic and strength properties required of geofoam block used in external stability analysis under seepage.

Sandy slopes are known to be susceptible to instability resulting from seepage flow (Fox et al., 2006, 2007; Wilson et al., 2007). Physical laboratory slope models have been successfully performed to evaluate seepage and infiltration induced slope stability problems (Fox et al., 2006; Lourenço et al., 2006; Chu-Agor et al., 2008; Ching-Chuan et al., 2009; Jia et al., 2009; Yan et al., 2010; Schnellmann et al., 2010; Lee et al., 2011). It is essential that potential seepage-induced instability of geofoam block slope systems is well understood by exploring behavior of physical models in order to design appropriate remedial solutions.

2. Materials and methods

2.1. Laboratory lysimeter studies

A total of 36 lysimeter experiments were performed in this study. Following Fox et al. (2006) and Wilson et al. (2007), the lysimeter was constructed using 1-cm-thick Plexiglas and had the dimensions of 200 cm length, 20 cm width, and 60 cm height to mimic field conditions of a slope under seepage in the laboratory (Fig. 1a). The reason for choosing a 200-cm lysimeter, which is longer than the 100-cm length slope used in the experiments (Fig. 1b), was to better represent the real field conditions where the failed mass of the slope often displaces to the toe of the slope and provides additional resistance to further displacement. The longer lysimeter also prevented the failed soil mass from exiting the soil compartment, thus allowing an accurate discharge measurement of seepage flow that was free of any suspended sediment at the outlet section. Such measurements were acquired using a digital scale placed at the outlet section of the lysimeter.

The lysimeter had a water reservoir located at one end. This reservoir was used to supply a constant water pressure head creating a hydraulic gradient in the slope and inducing seepage through the slope. Experiments started at the time water was supplied to the reservoir. Three different constant water pressure heads (25 cm, 38 cm, and 50 cm water pressure head) were supplied by overflow openings located on the wall of the water reservoir. Constant water pressure heads were maintained by feeding water into the reservoir via an inflow tube during the experiments. A stainless steel mesh having an opening size of 0.063 mm (equivalent to No. 230 sieve size) and a perforated 1-cm-thick Plexiglas plate with 8-mm diameter holes was placed between the reservoir and the soil compartment of the lysimeter. This type of a divider combination allowed resistance against the lateral forces created by these two compartments while preventing any soil entry into the water reservoir from the soil compartment during the sand placement and execution of the experiments.

During the experiments, pore-water pressures (h) generated by seepage flow inside the slope were measured by 22 pencil-size tensiometers (Soil Measurement Systems, Tucson, AZ, USA) installed on one side of the lysimeter (Fig. 1a). The porous cup of the tensiometers had an outside diameter of 0.67 cm and a length of 2.54 cm and was attached to a tube which was 7.5 cm long. The tube had a three-way valve with a pressure transducer attached on the

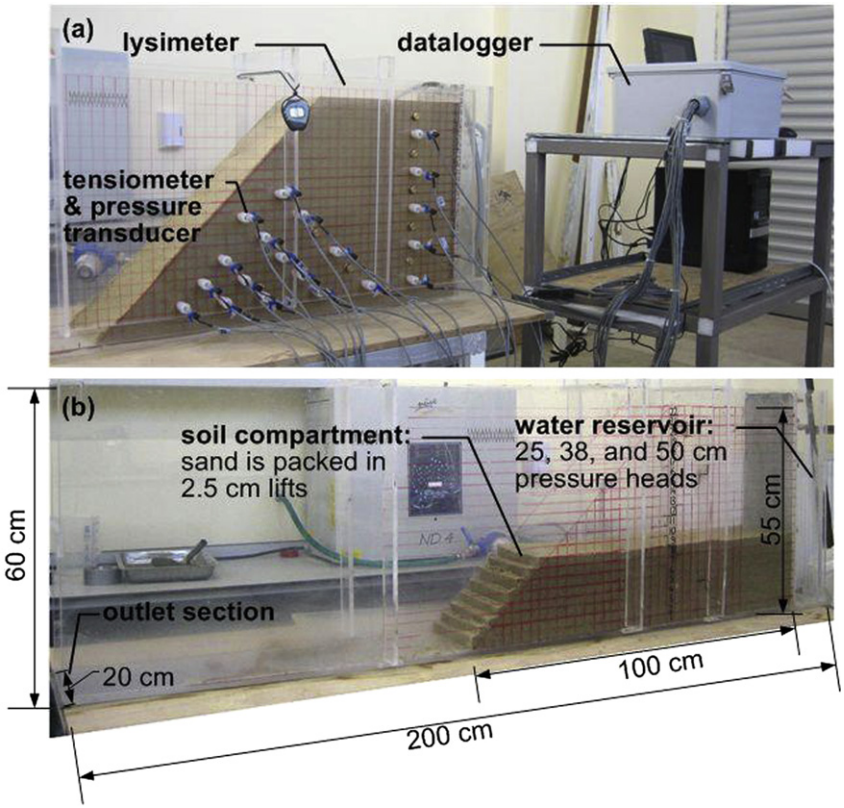

Fig. 1. (a) Laboratory setup included lysimeter, tensiometer, pressure transducer, and datalogger (b) soil packing in the lysimeter.

other end. These tensiometers were used in previous soil column studies and were effective for monitoring pore-water pressure dynamics (Akay and Fox, 2007). All tensiometers were equipped with bi-directional pressure transducers (ASDXRRX005PDAA5, Honeywell Sensing and Control, Golden Valley, MN, USA) capable of measuring pressure heads in a range from −345 cm-H_2O to +345 cm-H_2O (±5 psi). The data measured by the pressure transducers were collected at 10-s intervals by a datalogger (CR1000 w/multiplexer, Campbell Scientific, Logan, UT) for processing and storage. The locations of the tensiometers and their assigned numbers are given in Fig. 2. Experiments were performed until the tensiometer readings reached steady-state.

In addition to the soil pore-water pressure data collected by the datalogger and cumulative discharge collected by the digital scale, elapsed time from the start of an experiment to seepage initiation at the slope face (time of seepage) and time of final failure of a slope were recorded during an experiment. During the experiments, the physical condition of the slope was monitored with time using digital photography taken at preset intervals of one minute.

The soil was air-dried before each experiment to a moisture content value of 6–10 percent (measured according to ASTM D2216) to ensure uniform compaction. The soil placed in the soil compartment of the lysimeter was uniformly compacted in 2.5-cm lifts to obtain a single-layered slope with a dry density of 14 kN/m^3. The basal sand lift was compacted to a higher relative density for providing a leveling course (bedding sand) for geofoam blocks. The constructed slope had a 45° slope angle (1:1 horizontal:vertical) with the following dimensions: 100 cm length, 55 cm height, and 20 cm width (Fig. 1).

The sand properties were selected to be representative of granular fill material typically used in slopes and other civil engineering embankment applications (Table 1). The specific gravity

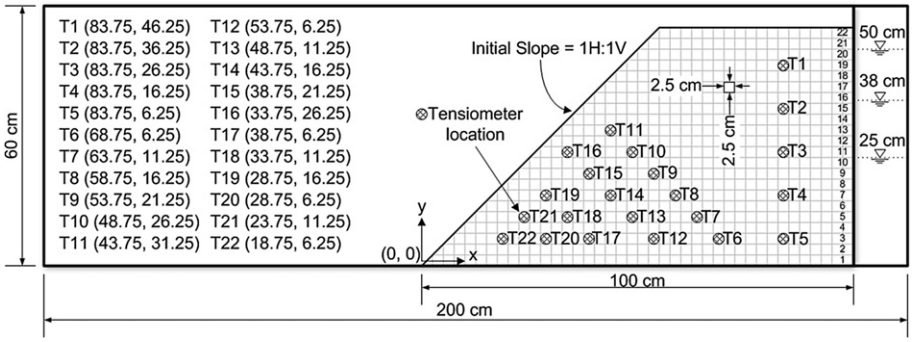

Fig. 2. Lysimeter showing location of tensiometers (x, y) given reference to the toe of the slope (0, 0).

Table 1
Material properties of soil and geofoam blocks used in the laboratory lysimeter experiments.

Property	Description & unit	Value
Material: sand		
Classification	Unified soil classification system	SP
Particle size distribution	Sand (%), Silt (%), Clay (%)	99.5, 0.5, 0.0
Effective size	D_{10} (mm)	0.2
Uniformity coefficient	C_u [−]	3.2
Coefficient of curvature	C_c [−]	1.2
Specific gravity	Gs [−]	2.60
Dry unit weight	γ_d (kN/m^3)	14
Cohesion	c' (kPa)	0
Angle of internal friction	ϕ' (degrees)	35
Material: EPS-block		
Dry unit weight	γ_d (kN/m^3)	1
Cohesion	c (kPa)	35
Angle of internal friction	ϕ (degrees)	30
Compressive strength	@ 5% strain (kPa)	142–148
	@ 10% strain (kPa)	160–167
Corrected initial young modulus	E (MPa)	7.0–7.1

was determined according to ASTM D854. The particle size distribution of the sand was measured according to ASTM D6913. Triaxial shear strength tests (TX) were conducted on both grab samples and undisturbed core samples extracted from the packed lysimeter via 20-cm long and 7.26-cm diameter undisturbed tubes according to ASTM D4767 to determine the strength properties of the material. Grab samples were compacted in the laboratory to achieve a dry density of 14 kN/m^3, which was the compaction effort used for the lysimeter physical slope models. The geotechnical properties of the sand were derived from triplicate samples and average values are presented in Table 1.

The hydraulic properties of the sand were determined from six undisturbed core samples (20-cm long, 7.26-cm diameter) extracted from the compacted lysimeter. The undisturbed samples were extracted randomly. Because of this, a simple internal control mechanism could be performed for quality assurance and quality check of the lysimeter compaction. Constant head permeability tests were conducted according to ASTM D2434 on the six cores which resulted in an average saturated hydraulic conductivity, K_{sat}, of 0.0285 cm/s (standard deviation, $\sigma = 0.003$ cm/s). The average dry density was equal to 13.97 kN/m^3 ($\sigma = 0.08$ kN/m^3).

The unsaturated soil hydraulic properties were determined by using the soil pore-water pressure head data collected from six undisturbed core samples (6.4-cm long, 7.26-cm diameter) extracted from compacted lysimeters, which were also selected randomly. In this method, the undisturbed cores were laboratory air-dried for one week before measuring their total weight using a digital scale and pore-water pressure head measurements obtained by a tensiometer inserted into the core. Following that, the water content of each core sample was gradually increased by slowly adding 5 mg of water using a syringe inserted into the core. The core sample was allowed to reach equilibrium (steady tensiometer readings) after each dose of water. Once at equilibrium, the pore-water pressure value was recorded, and another 5 mg of water was added to the core. This procedure was repeated until the cores were saturated (i.e., reached a condition where no more water could be injected without over spilling). After measuring the saturated weights, samples were oven dried and weighed to calculate the air-dried water content and the water content values for each step. The pairs of the measured pore-water pressures and the water content of the core samples (a total of 100 measurements from six cores) are presented in Fig. 3. The RETC (RETention Curve) computer code (van Genuchten et al., 1991) was used to predict the unsaturated soil hydraulic parameters of the soil. The curve fit of RETC (water retention curve) given in Fig. 3 was

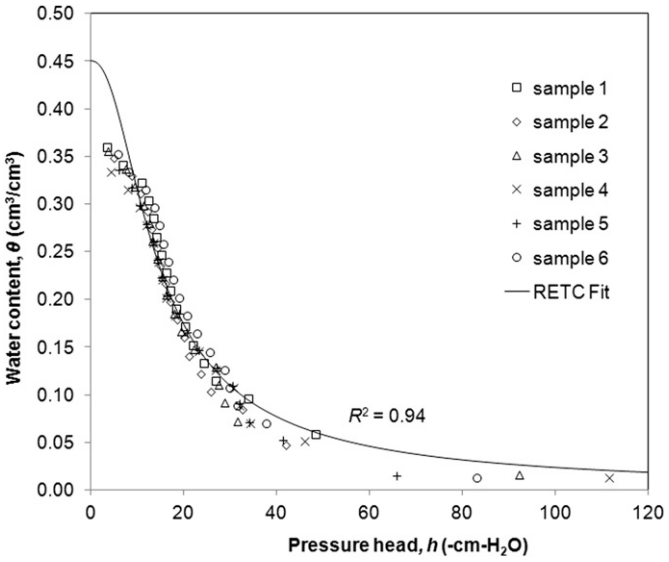

Fig. 3. Soil moisture characteristic curve of van Genuchten–Mualem model (van Genuchten, 1980) obtained by RETC using 100 test points.

generated by adapting the van Genuchten–Mualem model (van Genuchten, 1980):

$$\theta(h) = \begin{cases} \theta_r + \dfrac{\theta_s - \theta_r}{\left[1 + |\alpha h|^n\right]^m} & h < 0 \\ \theta_s & h \geq 0 \end{cases}$$

$$K(h) = K_{sat} S_e^l \left[1 - \left(1 - S_e^{\frac{1}{m}}\right)^m\right]^2$$

$$m = 1 - \frac{1}{n},\ n > 1$$

where θ_s is the saturated water content; θ_r is the residual water content; α [L^{-1}] is the inverse of the air-entry pressure (bubbling pressure); n is the pore-size distribution index; l is the pore-connectivity parameter (taken as 0.5); and $S_e = (\theta - \theta_r)/(\theta_s - \theta_r)$ is the effective saturation.

The R^2 value for the regression of measured versus fitted values was 0.94, which demonstrates a reasonable fit (Fig. 3). The van Genuchten parameters of the water retention curve used in numerical models are given in Table 2.

Table 2
Laboratory measured saturated hydraulic conductivity, K_{sat}, and soil–water retention parameters of sand and calibrated K_{sat} for lysimeter experiments.

	K_{sat} (cm s^{-1})	van Genuchten parameters[a]			
		θ_s [−]	θ_r [−]	α (cm^{-1})	n [−]
Laboratory measured parameters	0.0285	0.45	0.0	0.0944	2.3093
Calibrated K_{sat} for lysimeter experiments					
Matrix25cm10042012	0.0276	–	–	–	–
OneRow25cm13042012	0.0195	–	–	–	–
OneRowPartial Top25cm13042012	0.0222	–	–	–	–
OneRowPartial Bottom25cm10042012	0.0279	–	–	–	–

[a] θ_s = saturated water content, θ_r = residual water content, α = inverse of air-entry pressure (bubbling pressure), n = pore-size distribution index.

In addition to the soil used to construct the back-slope of the laboratory physical models, EPS-block geofoam was used as a lightweight fill material. The compressive resistance of geofoam block was determined using a series of three standard 50-mm cube samples according to ASTM D1621. Corrected initial Young Modulus, and the compressive resistance at 5 and 10% strains are given in Table 1.

Arellano et al. (2011a) have suggested that conventional limit equilibrium methods can be used to determine the factor of safety against slope failure of geofoam block slope systems. However, selection of the strength properties of geofoam block for numerical stability analysis has some uncertainties (Stark et al., 2004a; Arellano et al., 2011a). The modeling uncertainty is simply based on the fact that the geofoam block is not a traditional soil material. It is formed of discrete blocks that have a relatively high cohesive strength and a unique stress–strain behavior, including strain hardening and time-dependency, both of which are primarily based on the applied stress level. In addition, because the geofoam is placed as discrete blocks in the slope, there is a potential for relative block movement and interaction, which is not easily represented in limit equilibrium techniques. Complex failures, involving slip planes that engage both soil and geofoam block, may require more elaborate analysis methods (e.g., discrete element modeling), as discussed later.

Nonetheless, in order to evaluate a geofoam block slope system in using conventional limit equilibrium analysis, Arellano et al. (2011a) present five different alternatives for the selection of strength properties of the geofoam blocks. Our study selected 'Alternative 5' where both cohesion and internal friction angle was defined for the geofoam blocks. This alternative is based on

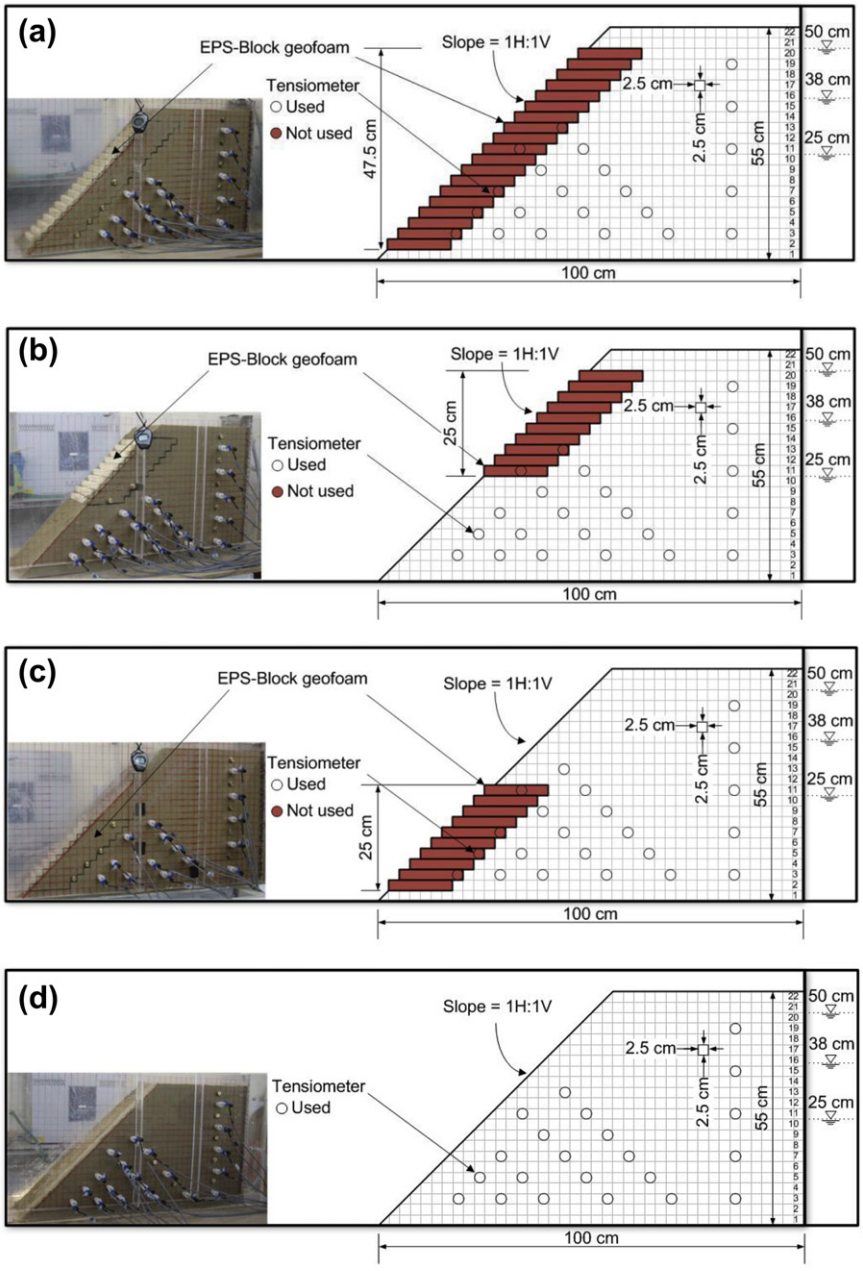

Fig. 4. Configurations tested during laboratory lysimeter experiments: (a) "One Row", (b) "One Row Partial Top", (c) "One Row Partial Bottom", and (d) "Matrix" (control experiment).

assuming that failure occurs through individual geofoam blocks as well as between geofoam blocks in a complex manner. Although not optimal, this alternative appeared to be the best alternative to represent the physical behavior of the laboratory slope models using simple limit equilibrium techniques. For the case where failure occurs through the EPS-blocks, Stark et al. (2004a) recommend using a cohesion value equal to one-quarter of the compressive strength at ten percent strain of the geofoam. If sliding occurs between EPS-blocks, EPS–EPS interface friction angle of 30° is recommended for routine design applications (Stark et al., 2004a). The geofoam block strength parameters used in this study are summarized in Table 1. In addition, Stark et al. (2004a) recommend using a conservative value of 1 kN/m^3 for the unit weight of EPS-blocks (actual unit weight was 0.24 kN/m^3) to take into account potential weight gain from long-term water absorption.

As discussed later, the presence of the geofoam blocks caused no restriction to the flow pattern during the experiments. Although geofoam blocks are essentially impermeable individually, they have a high transmissivity along block-to-block interfaces. The interfaces (joints) between the geofoam blocks resemble fractures inside an impervious rock or as apertures/macropores in a low permeable clayey soil medium. It is known that that fluid flow takes place predominantly through fractures in many geological formations with low matrix permeability (Zimmerman and Bodvarsson, 1996). Similarly, field studies showed that fractured clay and macroporous soils (dual-porosity medium comprised of macropore and soil matrix domains) have much larger composite saturated hydraulic conductivity compared to matrix domain alone (McKay et al., 1993; Villholth et al., 1998; Shipitalo et al., 2004; Baram et al., 2012). For these reasons, it was hypothesized that the composite (EPS + joints) hydraulic properties of the geofoam block system, as a whole, are similar to those of sand (Table 2) and therefore, sand's hydraulic parameters have been assigned to geofoam block domain in numerical models.

2.2. Slope configurations

Various geofoam block configurations are utilized to stabilize slopes (Arellano et al., 2011a,b). Three different configurations were tested in this study where the geofoam blocks were placed on the face of the compacted sandy slope. The block layouts used in this study were selected based on typical construction practice and conceptual alternatives for block placement. The geofoam blocks used in the laboratory lysimeter tests were: 2.5-cm high, 5-cm wide, and 15-cm long to ensure a 1:20 scale of a geofoam block which corresponds to a commonly manufactured size.

The first configuration tested in the laboratory is referred to as "One Row" (Fig. 4a). This type of usage is encountered in the construction of geofoam block fills placed adjacent to existing side slope in hilly areas, or adjacent to an existing roadway embankment which has a trapezoidal cross-section. This case was replicated in the laboratory by placing the geofoam blocks on top of each other along the slope face.

Another common remediation strategy used in construction of highway embankments is to replace the upper portions of the earthen fill with geofoam blocks to reduce the driving forces available for slope instability. This remediation technique was used in slope stability problem encountered in Trunk Highway A located within Bayfield County in northern Wisconsin (Reuter and Rutz, 2000) and Route 23A, Jewett County, New York (Jutkofsky et al., 2000). This case was reproduced by placing the geofoam blocks on the upper portion of the slope face. This configuration is referred to as "One Row Partial Top" (Fig. 4b).

Severe seepage can cause subsurface erosion resulting in undercutting of slopes (Fox and Wilson, 2010). Seepage forces intensify at the toe of the slopes and can be of sufficient magnitude to initiate particle movement that can lead to a global failure. Since geofoam block is a non-erodible material, a third layout referred to as "One Row Partial Bottom" was tested in which geofoam blocks were placed at the toe of the slope where the seepage forces intensify (Fig. 4c).

To compare and evaluate the behavior of these three systems, a control experiment was also conducted in which single-layered sand was compacted into the lysimeter with no geofoam blocks placed on the slope face. This configuration is referred as to "Matrix" (Fig. 4d).

It should be noted that all configurations were run in triplicate to ensure the repeatability of the experimental setup. The list of the 36 lysimeter experiments can be found in Table 3. A naming convention was used to distinguish the experiments so that the title of the experiment included the configuration type, constant pressure head of the boundary condition, and the date of the experiment (ddmmyyyy), respectively.

2.3. Numerical model simulations

Numerical model simulations (variably saturated flow modeling and slope stability modeling) were performed to quantify the results observed in the laboratory lysimeter experiments. For this reason, calibration of the hydraulic parameters of the soil used in variably saturated flow modeling is necessary. Calibration was performed to match the observed hydrological response of the laboratory lysimeter experiments to the computed response of the numerical models by adjusting the hydraulic parameters of the soil. In this study, this was achieved by the inverse estimation of only K_{sat} so that the computed cumulative discharge matched the measurements taken during the experiments. The other soil parameters defining the unsaturated characteristics of the soil (van Genuchten (1980) model parameters) were fixed to their laboratory measured values and hence excluded from the inverse estimation process.

For initial flow modeling to calibrate K_{sat}, the HYDRUS finite-element computer model was used which solves the Richards equation for saturated–unsaturated water flow and convection–dispersion type equations for heat and solute transport (Šimůnek et al., 2012). HYDRUS executes the inverse estimation of the hydraulic properties by implementing a Marquardt–Levenberg nonlinear method which has become a standard in nonlinear least-square fitting among soil scientists and hydrologists (Šimůnek and van Genuchten, 1997). During the inverse estimation, the initial estimates of the soil parameters are iteratively improved to minimize an objective function which expresses the discrepancy

Table 3
List of the laboratory lysimeter tests.

Configuration	Constant Water Head Level		
	25 cm	38 cm	50 cm
Matrix	29112011	06122011	25112011
	30122011	03012012	07032012
	10042012[a]	20042012[a]	04042012[a]
One Row	02122011	20122011	01112011
	05012012	05012012	13022012
	13042012[a]	08052012[a]	04052012[a]
One Row Partial Bottom	08122011	28122011	15112011
	10012012	18012012	17012012
	10042012[a]	20042012[a]	04042012[a]
One Row Partial Top	13122011	13122011	15122011
	26012012	16122011	31012012
	13042012[a]	27042012[a]	27042012[a]

[a] Last set of the triplicate experiments were tested with the pore-water pressure measurement setup installed.

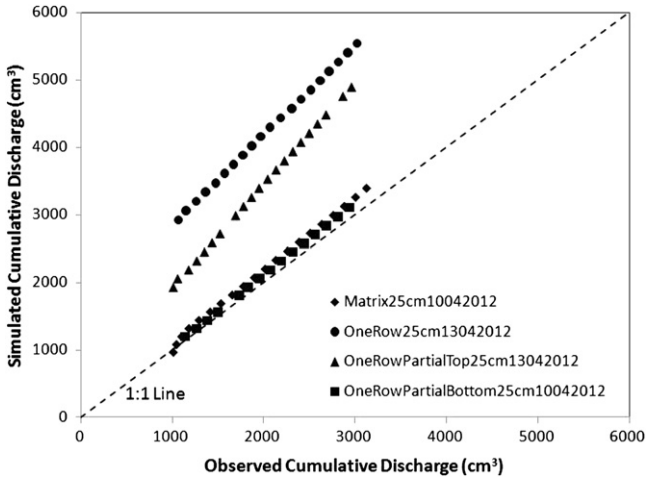

Fig. 5. Observed versus HYDRUS predicted cumulative discharge for four lysimeter experiments before calibration on saturated hydraulic conductivity (K_{sat}).

between the observed values and the predicted system response (Šimůnek and van Genuchten, 1996). In this study, an objective function comprised of deviations between measured and predicted cumulative discharge across the seepage boundary was minimized by adjusting only K_{sat}. HYDRUS iteratively improved the initial estimate of K_{sat} (laboratory measurement of 0.0285 cm/s given in Table 2) as long as the sum of squared deviations decreases (i.e. minimization of the objective function) until a local minimum is reached, then optimization was stopped.

Nash–Sutcliffe model efficiency coefficient (NS), a quantitative statistic, was calculated to assess the predictive ability of the calibration model for each configuration. NS indicates how well the plot of observed versus simulated data fits the 1:1 line (Moriasi et al., 2007). Also known as the coefficient of determination, the non-dimensional NS model efficiency coefficient was calculated as follows:

$$\mathrm{NS} = 1 - \frac{\sum_{i=1}^{n}\left(Y_i^{obs} - Y_i^{sim}\right)^2}{\sum_{i=1}^{n}\left(Y_i^{obs} - Y^{mean}\right)^2}$$

where Y_i^{obs} is the ith observed cumulative discharge, Y_i^{sim} is the ith simulated cumulative discharge, and Y^{mean} is the mean of observed cumulative discharge. Root mean square error (RMSE) of measured and HYDRUS simulated soil–pore-water pressure head was calculated for each tensiometer as follows:

$$\mathrm{RMSE} = \sqrt{\frac{\left(T_i^{obs} - T_i^{sim}\right)^2}{n}}$$

where T_i^{obs} is the ith observed pore-water pressure head, and T_i^{sim} is the ith simulated pore-water pressure head.

Following the calibration process, the lysimeter experiments were simulated using the coupled SEEP/W (saturated/unsaturated

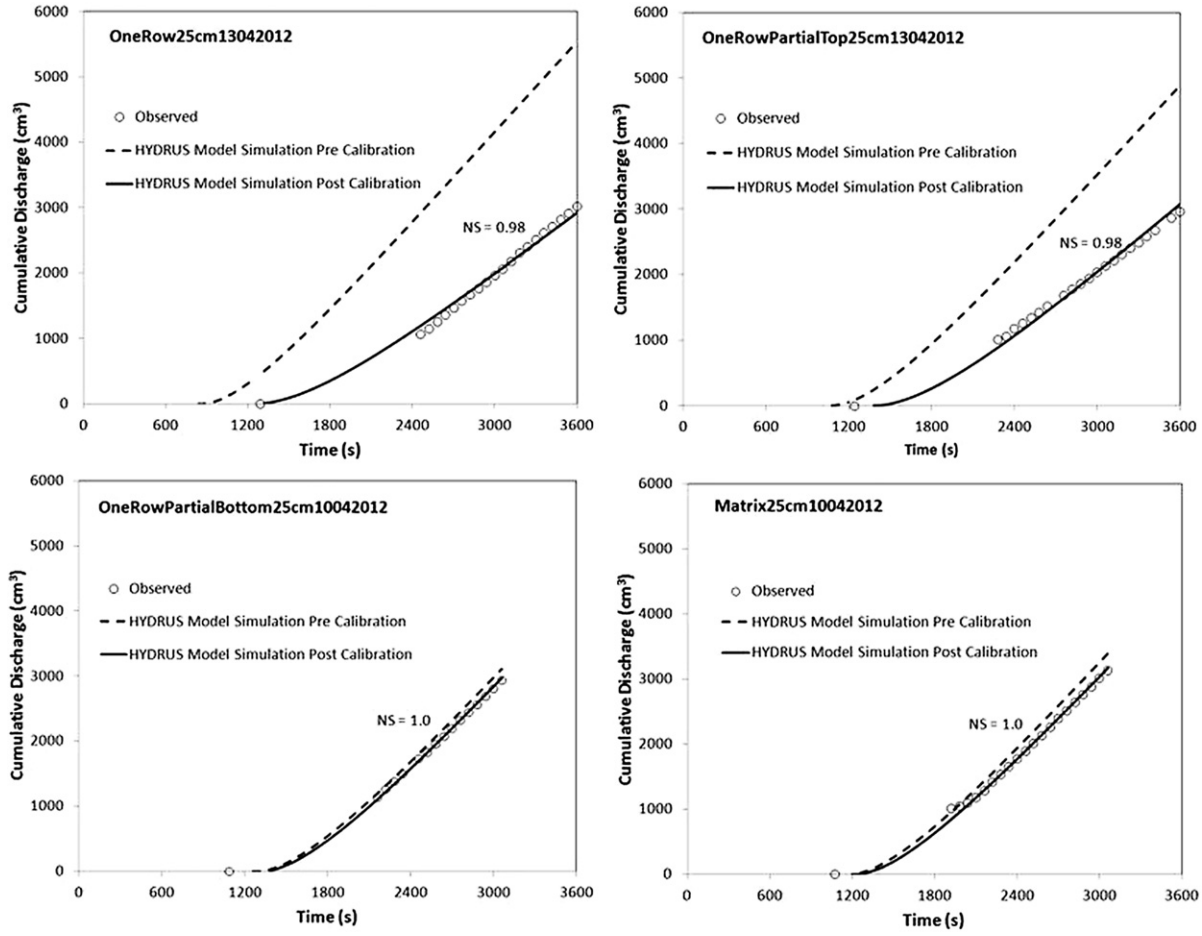

Fig. 6. Cumulative discharge curves for four lysimeter experiments before and after calibration on saturated hydraulic conductivity (K_{sat}).

flow model) and SLOPE/W (slope stability model) computer programs. SEEP/W, similar to HYDRUS, is a finite-element model solving Richards equation for two-dimensional variably saturated flow (Geo-Slope International, 2009). Using the calibrated K_{sat} values for each configuration and the unsaturated soil hydraulic parameters (Table 2), transient seepage simulations were performed using SEEP/W in order to predict the location of the phreatic surface and pore-water pressure distributions during the experiments.

In order to perform transient seepage analyses, the initial pressure head distribution needed to be defined for SEEP/W and HYDRUS. This was achieved by prescribing a single pore-water pressure head for the computational domain that was constructed to represent the geometry of the lysimeter. The initial pressure head of the computational domain to start the simulation was calculated by averaging the tensiometer pressure head readings collected at the start of the laboratory experiments.

The boundary condition types for the numerical models were selected according to the physical conditions of the lysimeter setup. A constant pressure head boundary was used for the water reservoir of the lysimeter. The prescribed pressure heads were 25 cm-H_2O, 38 cm-H_2O, and 50 cm-H_2O (hydrostatic pressure head measured to the reference plane passing through the base of the slope) which were constant during the execution of the models. A seepage face boundary condition was specified along the face of the slope (1:1 Horizontal:Vertical). A seepage face boundary acts as a zero pressure head boundary for nodes that are saturated and a no-flux boundary for nodes that are unsaturated (Akay et al., 2008). A no-flux boundary was selected for the bottom of the computational domain to simulate the impervious base of the lysimeter. The simulation times of the numerical models were the same as their associated laboratory lysimeter experiment.

After the transient seepage analyses were completed, the results were imported into SLOPE/W which uses a conventional limit equilibrium analysis to determine slope stability (Geo-Slope International, 2008). SLOPE/W implements various limit equilibrium models (LEM). For LEM practice, Krahn (2003) recommended using Morgenstern and Price (1967) or Spencer (1967) methods since these methods satisfy both force and moment equilibrium. Also, the Spencer's (1967) method was recommended by Wright (1969) after examining eight different LEM. In addition, Duncan and Wright (1980) indicated that Spencer's method provides the best estimate of Factor of Safety (FS). In this study, all the reported FS values using LEM are calculated using the Spencer method.

The auto-locate function of SLOPE/W was first utilized to define the potential failure surface. The auto-locate function's tendency to find the most probable slip surface with the minimum FS value resulted in discrepancies compared to observed laboratory failure planes. Therefore, the entry–exit function of SLOPE/W was used in which the ranges of entry and exit locations of trial slip surfaces were specified to run slope stability models. Based on the observed laboratory failure planes, entry range with specified increments either on the crest or along the face of the slope and an exit point at the toe of the slope were selected. As a result, SLOPE/W generated potential slip surfaces that are comparable with observed laboratory failure planes. The FS of the failure plane which closely matched the actual laboratory failure plane was reported in this study.

3. Results and discussion

3.1. Model calibration

Cumulative discharge measurements were acquired only for experiments which failure did not cause a drastic change in the slope face compared to its initial condition (1:1 slope angle). There are two reasons for this selection: 1) since these measurements would be used for the calibration of K_{sat} using HYDRUS, the computational domain geometry should be the same as the laboratory slope packed in the lysimeter. However, a failed slope would be much different than its associated numerical model. For this reason, experiments with only small, if any, deviations compared to the computational domain were used; 2) cumulative discharge measurements were taken by using a digital scale located at the outlet section of the lysimeter which weighed the seepage flow exiting from the slope. Failure of a slope increases the probability of sediment influx at the outlet of the lysimeter. For this reason, the sediment influx should be minimal in order to convert the weights directly to volumes of water. For the experiments selected for calibration of each configuration (Table 2), various measurements

Table 4
Root mean square error (RMSE), in cm H_2O, between measured and simulated soil pore-water pressure at tensiometer locations[a] in each lysimeter experiment before calibration and after calibration on saturated hydraulic conductivity, K_{sat}.

Lysimeter experiment (Configuration, Water Head & Date)	Tensiometers										
	1	2	3	4	5	6	7	8	9	10	11
	12	13	14	15	16	17	18	19	20	21	22
(a) Prior to calibration											
Matrix25cm10042012	2.6	4.1	1.4	1.0	1.1	11.9	5.9	0.7	1.5	1.8	1.2
	0.7	0.6	1.0	1.5	2.7	1.1	1.7	2.4	7.1	1.3	2.6
OneRow25cm13042012	4.6	0.8	1.6	1.6	2.2	2.2	2.5	2.6	3.1	4.1	–
	3.7	3.6	3.3	3.6	–	3.4	2.6	–	4.9	–	–
OneRowPartialBottom25cm10042012	9.6	9.6	2.1	1.2	1.5	1.1	1.4	1.2	2.4	3.8	7.4
	1.8	1.1	2.1	1.8	–	3.5	1.7	–	3.6	–	–
OneRowPartialTop25cm13042012	2.1	3.4	2.0	0.9	1.3	1.1	0.6	0.7	2.1	5.1	–
	1.0	1.3	1.5	2.3	–	1.7	1.6	2.5	1.3	2.1	1.3
(b) Calibration on K_{sat}											
Matrix25cm10042012	2.7	4.1	1.4	0.9	1.1	11.8	5.7	0.7	1.5	1.7	1.1
	0.9	0.7	1.0	1.4	2.8	1.3	1.9	2.5	7.1	1.4	2.8
OneRow25cm13042012	3.5	0.9	1.1	0.8	1.3	1.0	1.1	1.3	1.8	3.4	–
	2.0	2.3	2.1	2.5	–	3.4	2.6	–	2.9	–	–
OneRowPartialBottom25cm10042012	9.6	9.6	2.1	1.2	1.5	1.2	1.5	1.2	2.4	3.7	7.4
	1.9	1.2	2.0	1.7	–	3.5	1.7	–	3.7	–	–
OneRowPartialTop25cm13042012	2.3	3.4	1.6	0.4	0.8	0.6	1.2	1.1	1.2	4.3	–
	1.3	0.9	1.6	1.3	–	1.7	1.3	1.9	2.3	1.3	2.1

[a] Some tensiometers were not used depending on the configuration tested. Please refer to Fig. 2 for the location of tensiometers 1–22 and Fig. 4 for the tensiometers used for each of the configuration.

of sediment concentrations in the seepage flow at the outlet section of the lysimeter revealed negligible amounts of sediment entrapment (as low as 1.24 g/L).

Because the changes in slope physical conditions were minimal for the experiments with 25 cm-H_2O constant pressure head boundary condition, experiments listed in Table 2 were chosen for the calibration of each configuration. The calibration model of HYDRUS consisted of a finite-element grid of 1275 mesh nodes and 2437 triangular mesh elements. Minimum time step used during the execution of the model was 0.1 s. For the initiation of the calibration process outlined earlier, the laboratory measurement value of 0.0285 cm/s was used as the initial estimate of the K_{sat} value. HYDRUS computed discharge values using the initial estimate versus laboratory observed discharge measurements are presented in Fig. 5. Strong linear dependence (Pearson product moment correlation coefficient value almost equal to 1) between the measured and the model values of the seepage discharge were observed for each configuration (Fig. 5). Considering this strong relationship, the most essential parameter that effects the time to seepage and magnitude of the seepage discharge (flux rate), K_{sat}, was selected as the only soil parameter to be calibrated.

The calibrated values of K_{sat} for each configuration were given in Table 2. The resultant cumulative discharge curves are presented in Fig. 6. Using the calibrated values of K_{sat}, the numerical model made good predictions for both the time of seepage and the cumulative discharge. High values of NS (a value of 1 reveals a perfect match of modeled discharge to the observed data) for all configuration tests

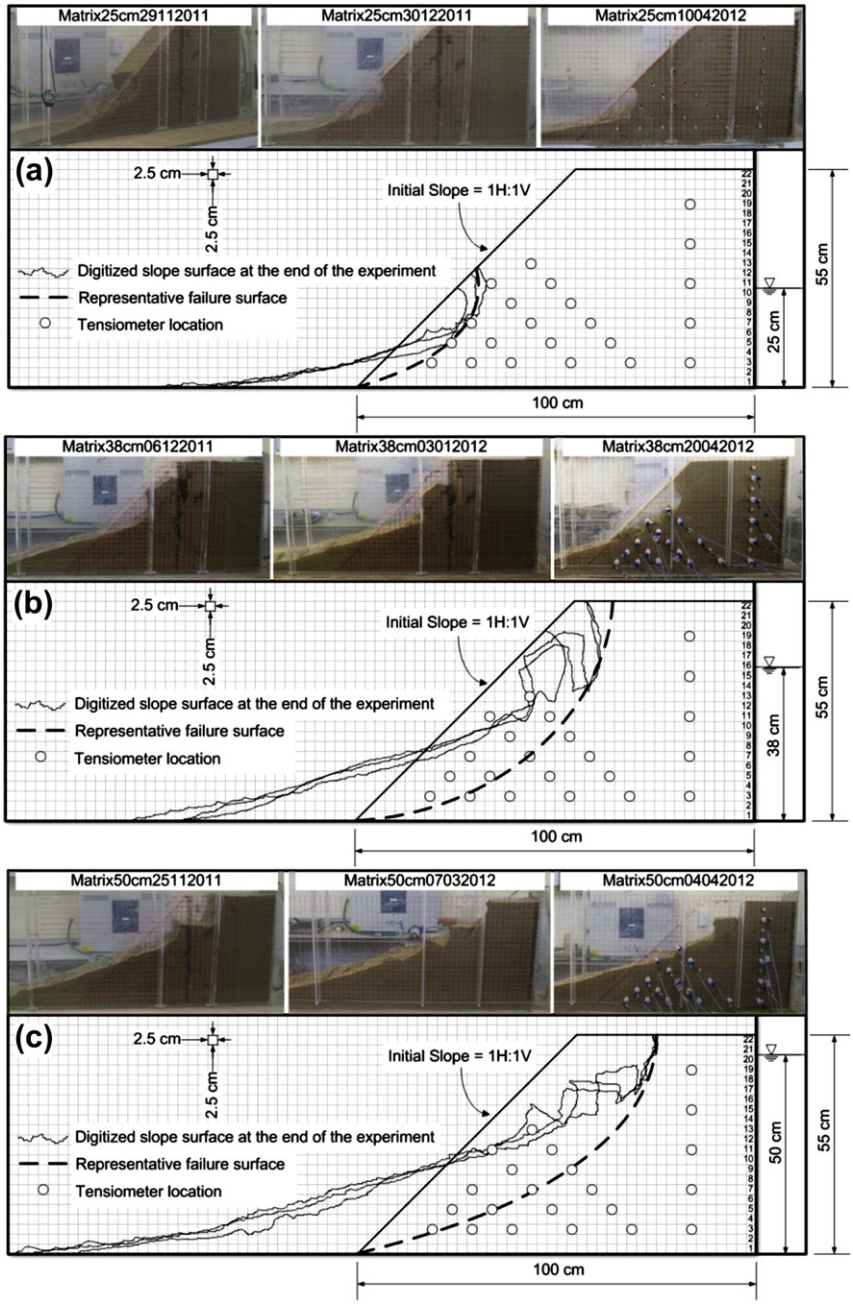

Fig. 7. Slope physical conditions and representative failure surfaces at the end of the triplicate experiments of Matrix configuration under (a) 25 cm- (b) 38 cm-, and (c) 50 cm-H_2O pressure head boundary conditions.

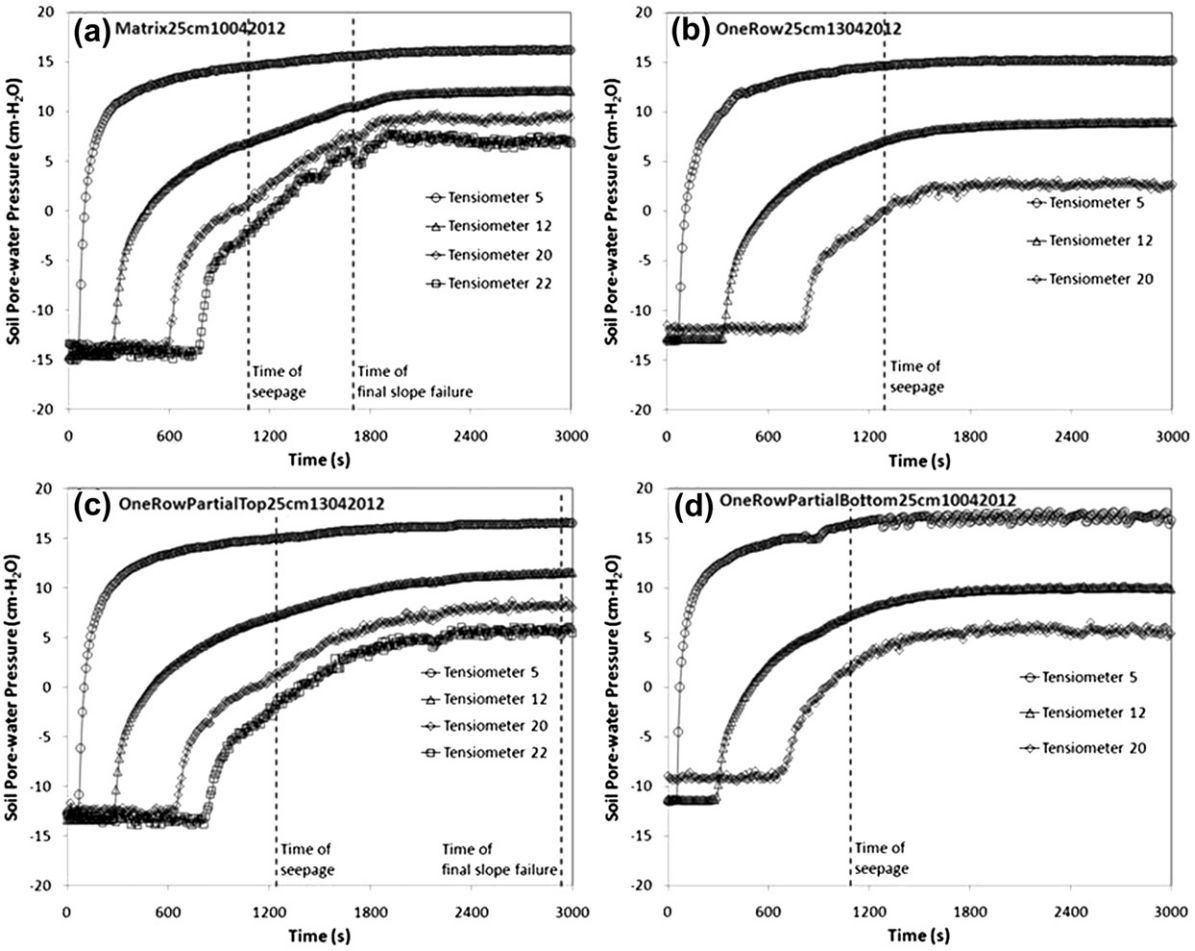

Fig. 8. Tensiometer readings during four lysimeter experiments.

revealed an acceptable level of performance of the calibration model of HYDRUS (Fig. 6).

The calibration process also helped to better predict the pore-water pressures that developed within the slope during the experiments. Accurate pore-water pressure values are essential to compute reliable FS values for each configuration under certain constant pressure head boundary condition. RMSEs are outlined in Table 4 for prior calibration and after calibration on K_{sat}. Since the pre-calibration and post-calibration value of K_{sat} is similar (Table 2), no noticeable improvement has been detected for Matrix and One Row Partial Bottom experiments. Overall, calibrating only on K_{sat} also provided a reasonable fit for pore-water pressures that developed within the slope (average RMSE = 2.3 cm-H_2O).

3.2. "Matrix" configuration

The final slope faces of the "Matrix" configuration were digitized at the end of the experiments for each boundary condition (Fig. 7). As a result, triplicate experiments showed that the 'final slope surfaces' (refers to the physical condition of the slope at the end of the experiment) were similar for a specific pressure head boundary

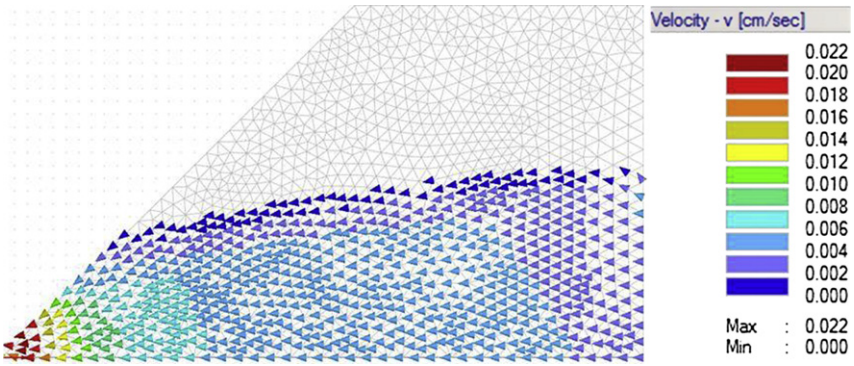

Fig. 9. Direction and magnitude of seepage flow simulated for the saturated zone under 25 cm-H_2O pressure head boundary condition by HYDRUS.

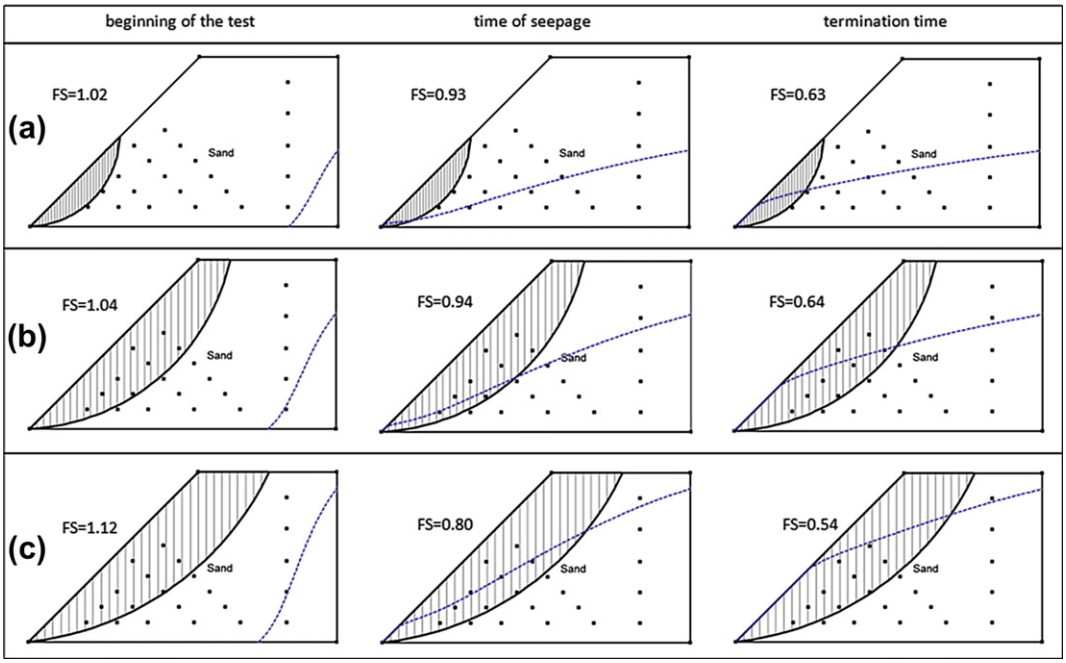

Fig. 10. Factor of safety (FS) of the "Matrix" configuration and the location of the phreatic surface at three different time intervals under (a) 25 cm-, (b) 38 cm-, and (c) 50 cm-H_2O pressure head boundary conditions.

condition and proved that the results of the experiments were repeatable. Associated with the final slope surfaces, representative failure surfaces (the failure surface for which FS values were calculated) were also depicted. The experiments were terminated (termination time) after the support of failed soil mass at the toe of the slope equilibrated with the driving forces (time of final slope failure), hence no more progressive failure occurred. At this stage of the experiments, tensiometer readings also reached steady-state as

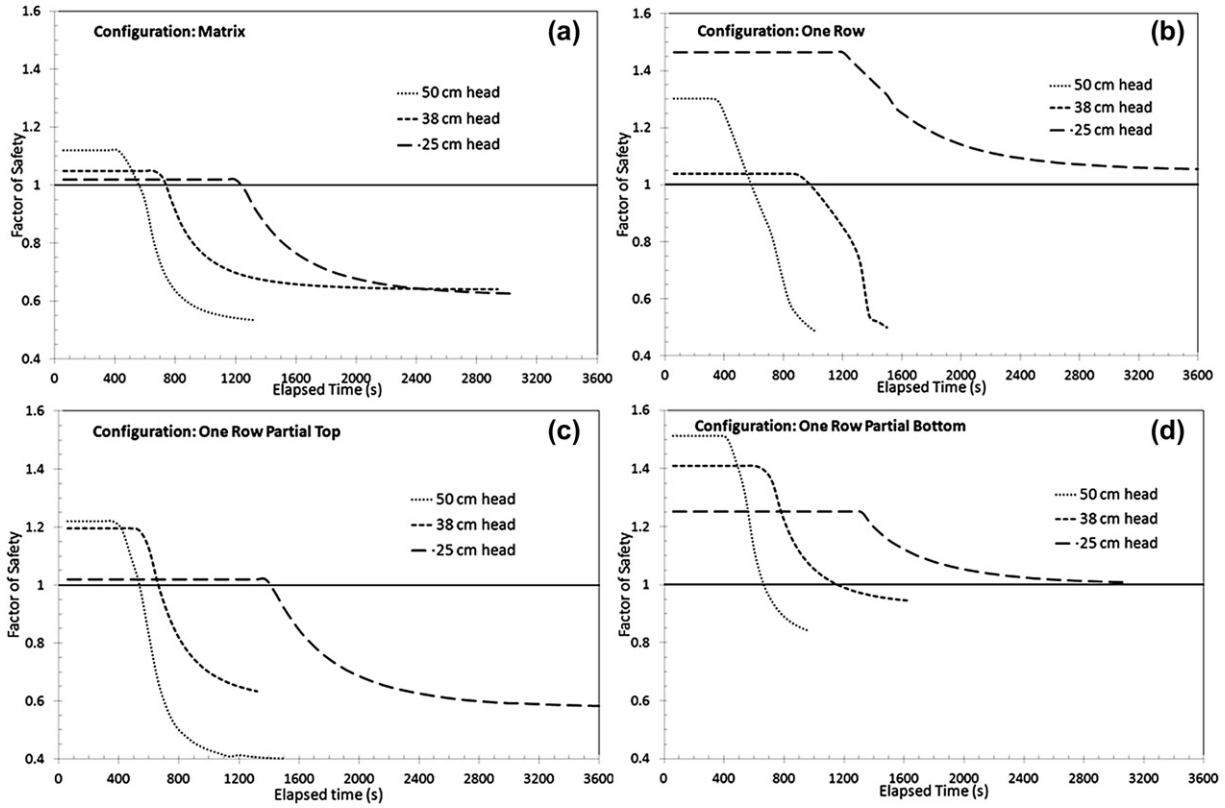

Fig. 11. Change in Factor of safety (FS) with time under three different boundary conditions for the (a) "Matrix", (b) "One Row", (c) "One Row Partial Top", and (d) "One Row Partial Bottom" configurations.

demonstrated in Fig. 8a. In this figure, four tensiometers were selected to monitor the pore-water pressure time-series near the inflow reservoir of the lysimeter (Tensiometer 5), approximately half the distance from the inflow reservoir to slope face (Tensiometer 12), and at the toe section of the slope (Tensiometers 20 & 22).

For a 25 cm-H_2O pressure head boundary condition, the final slope surface entered at the face of the initial 1:1 slope (Fig. 7a); whereas for the 38 cm-H_2O and 50 cm-H_2O boundary conditions, the failure surface entered at the crest (distance to slope break was approximately 9.5 cm, and 19.5 cm, respectively) (Fig. 7b and c). The exit location of the failure surfaces created by each boundary condition was selected as the toe of the slope where the initiation of all failures was started because of the intensified seepage forces at the toe section as seen in Fig. 9. By extending the upper portion of the final slope surface to the toe of the slope, failure surfaces were created (Fig. 7). Since the failure surface of the 25 cm-H_2O pressure head boundary condition enters from the slope and exit at the toe (Fig. 7a), this type of failure was referred to as 'shallow-seated failure', whereas the other failure surfaces which entered from the crest and exited at the toe (Fig. 7b and c) were referred to as 'deep-seated failures'.

The FS values were calculated for the failure surfaces that were obtained from laboratory experiments (Fig. 7) by using SLOPE/W slope stability model. The progress of the phreatic surface and associated FS values at three different times are given in Fig. 10. The decrease in FS can immediately be realized as soon as seepage flow enters into the failure plane and failure (i.e. FS < 1) coincides with initial daylighting of seepage at toe of slope. Since the steady-state phreatic surface generated by the 50 cm-H_2O boundary condition enveloped a larger zone inside the slope and so the removal of the suction pressures, its failure surface extends more into the slope compared to other failure surfaces (Fig. 10). The change in FS throughout the experiment can be found in Fig. 11a. The variance in FS at the beginning of the experiment was due to the difference in the failure surfaces and initial suction conditions.

3.3. "One Row" configuration

The final slope surfaces of the triplicate experiments of the "One Row" configuration are given in Fig. 12. The repeatability of the lysimeter experiments was noted since the final slope surfaces were similar for each boundary condition (Fig. 12a–c). Considering the final slope surfaces obtained at the end of the experiments, hypothesized failure surfaces (entering from the crest and exiting at the toe of the slope) were indicated for each experiment with 38 cm-H_2O and 50 cm-H_2O boundary conditions. In contrast to the "Matrix" configuration which showed a shallow-seated failure (Fig. 7a), the slope stayed intact under seepage force effects created by the 25 cm-H_2O pressure head boundary condition for each of the triplicate experiments (Fig. 12a). When the representative failure surface of the "Matrix" configuration under 25 cm-H_2O boundary condition (Fig. 7a) was superimposed onto the "One Row" configuration (Fig. 12d), it can be seen that the shallow-seated failure surface stayed within the geofoam blocks. Confirming the laboratory observations which showed no failure (Fig. 12a), SLOPE/W calculated relatively high FS for this failure surface since the strength properties of geofoam block (Table 1) governs the

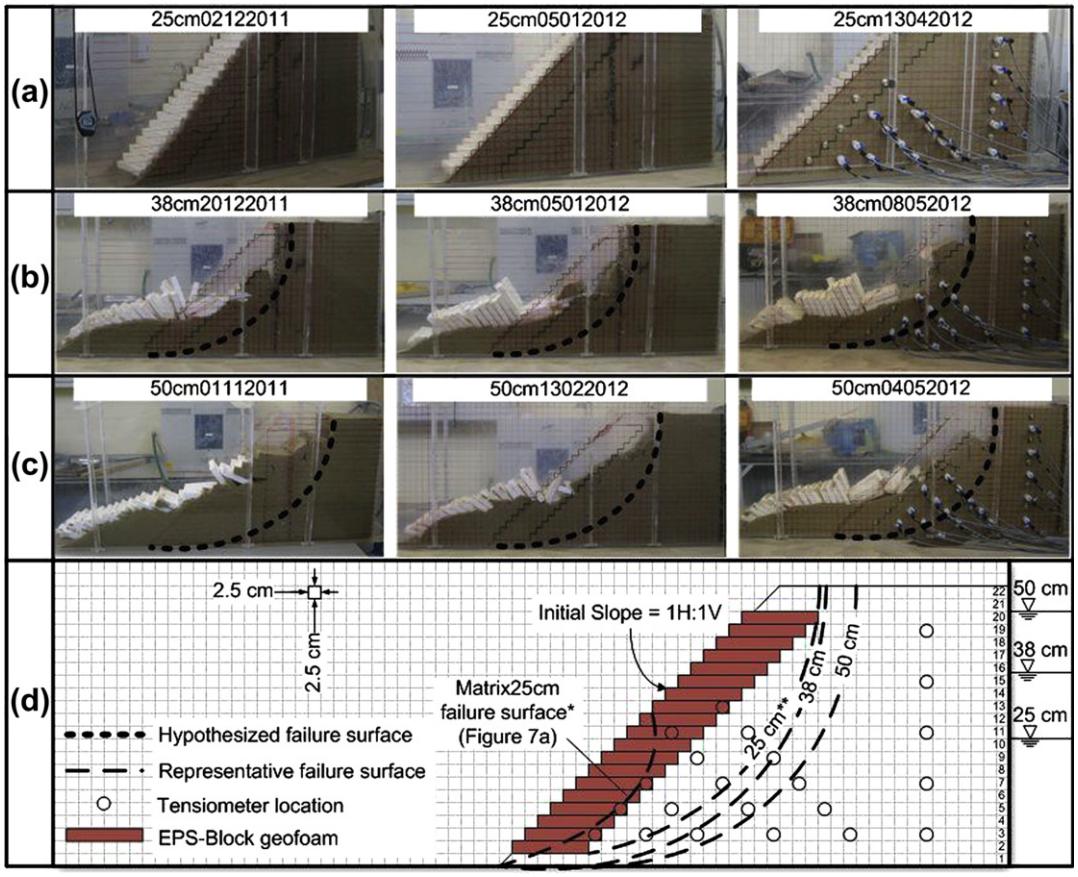

Fig. 12. Slope physical conditions and hypothesized failure surfaces at the end of the triplicate experiments of "One Row" configuration under (a) 25 cm-, (b) 38 cm-, and (c) 50 cm-H_2O pressure head boundary conditions. (d) Representative failure surfaces for each boundary condition.

calculation of FS (a cohesive failure through geofoam blocks is unlikely) in the simplified approach. This experiment showed that replacement of the soil mass that is typically dislodged during a shallow-seated failure with the lightweight and non-erodible EPS-block geofoam, significantly improves the stability of the slope.

Since both laboratory lysimeters experiments (Fig. 12a) and SLOPE/W did not show a failure through geofoam blocks under a 25 cm-H_2O pressure head boundary condition, a failure surface which was located immediately behind the geofoam blocks was selected (indicated as "25 cm**" in Fig. 12d). FS values were reported for this more "deep-seated" failure surface in Fig. 13a. The change in FS with time during the experiment for this failure surface can be found in Fig. 11b. It can be seen that the FS value remained above 1.0 throughout the experiment (Fig. 11b), even when steady-state conditions were well established (Fig. 8b).

Similar to the "Matrix" configuration, failure surfaces resulted from 38 cm-H_2O and 50 cm-H_2O pressure head boundary conditions were "deep-seated" failures as shown by hypothesized failure surfaces given in Fig. 12b and c, respectively. The FS values calculated by SLOPE/W for the representative failure surfaces (representation of the hypothesized failure surfaces of the triplicates) given in Fig. 12d at the end of the experiments were 0.50 and 0.48 for the 38 cm-H_2O and 50 cm-H_2O pressure head boundary conditions, respectively (Fig. 13b and c).

3.4. "One Row Partial Top" configuration

The final slope surfaces of the triplicate experiments of the "One Row Partial Top" configuration are given in Fig. 14. The repeatability of the lysimeter experiments was noted since the final slope surfaces were similar for each boundary condition (Fig. 14a–c). Considering the final slope surfaces obtained at the end of the experiments, hypothesized failure surfaces were indicated for each experiment. Similar to the "Matrix" configuration, shallow-seated failure was observed at the end of the triplicate experiments, only this time the entrance of the representative failure surface on the slope face went down about 5 cm when compared to the entrance point of the "Matrix25cm" representative failure surface (Fig. 14d). This entrance point coincided with the base of the geofoam block layer located in lysimeter layer 11 (Fig. 14d). Apparently, the final slope surface adjusted itself so that the shallow-seated failure would not go through the geofoam blocks. Confirming the laboratory observations, SLOPE/W calculated FS >1.0 for the "Matrix25cm" representative failure surface which passed partially through the geofoam blocks (Fig. 14d) for the "One Row Partial Top" configuration under a 25 cm-H_2O boundary condition. The FS values given in Fig. 15a were calculated for the representative failure surface of the 25 cm-H_2O boundary condition (Fig. 14d). The change in the FS value during the experiment was given in Fig. 11c, where the FS value of 1.02 calculated at the initial condition decreased to 0.98 at the time of seepage, and to 0.58 at the end of the experiment. It should be noted that steady-state conditions were reached at the end of the experiment (Fig. 8c).

Similar to "Matrix" and "One Row" configurations, failure surfaces for the 38 cm-H_2O and 50 cm-H_2O pressure head boundary conditions were also deep-seated failures as shown by hypothesized failure surfaces given in Fig. 14b and c, respectively. The FS values calculated by SLOPE/W for the representative failure surfaces given in Fig. 14d at the end of the experiments were 0.63 and 0.40 for 38 cm-H_2O and 50 cm-H_2O pressure head boundary conditions, respectively (Fig. 15b and c).

3.5. "One Row Partial Bottom" configuration

The final slope surfaces of the triplicate experiments of the "One Row Partial Bottom" configuration are given in Fig. 16. The repeatability of the lysimeter experiments was noted since the final slope surfaces were similar for each boundary condition (Fig. 16a–c). Similar to "One Row" configuration, the slope was stable and showed no failure for a 25 cm-H_2O boundary condition. When the representative failure surface of the "Matrix" configuration under a 25 cm-H_2O boundary condition (Fig. 7a) was superimposed onto

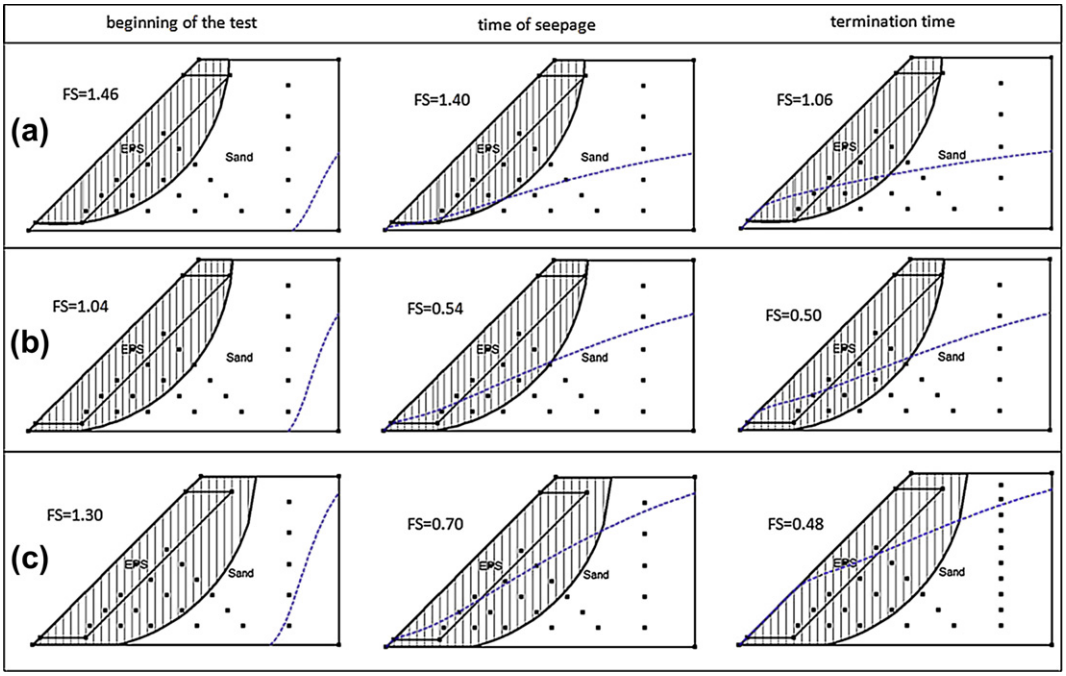

Fig. 13. Factor of safety (FS) of the "One Row" configuration and the location of the phreatic surface at three different time intervals under (a) 25 cm-, (b) 38 cm-, and (c) 50 cm-H_2O pressure head boundary conditions.

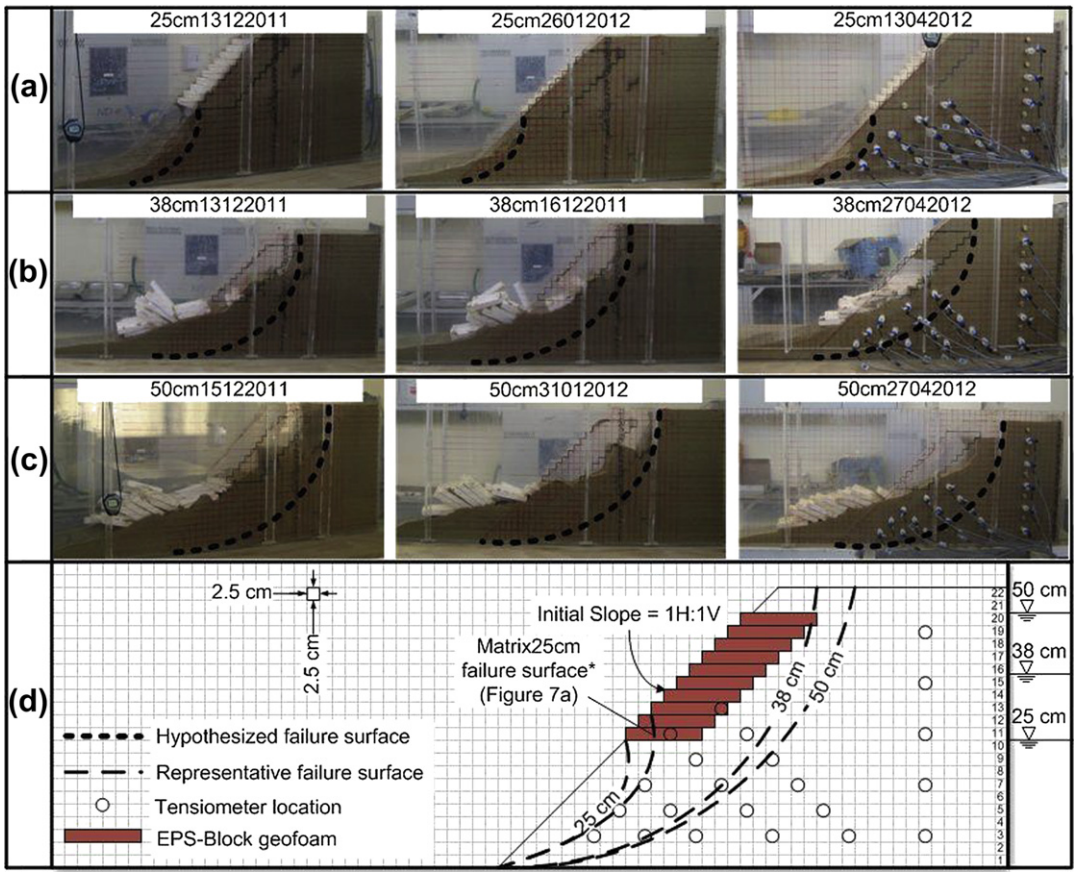

Fig. 14. Slope physical conditions and hypothesized failure surfaces at the end of the triplicate experiments of "One Row Partial Top" configuration under (a) 25 cm-, (b) 38 cm-, and (c) 50 cm-H_2O pressure head boundary conditions. (d) Representative failure surfaces for each boundary condition.

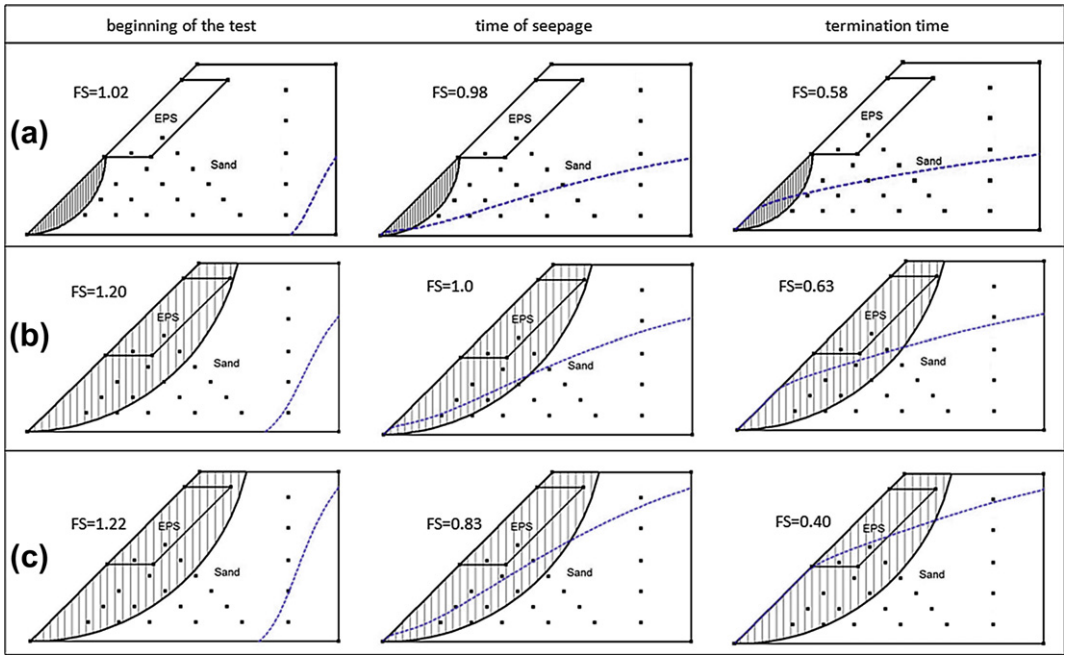

Fig. 15. Factor of safety (FS) of the "One Row Partial Top" configuration and the location of the phreatic surface at three different time intervals under (a) 25 cm-, (b) 38 cm-, and (c) 50 cm-H_2O pressure head boundary conditions.

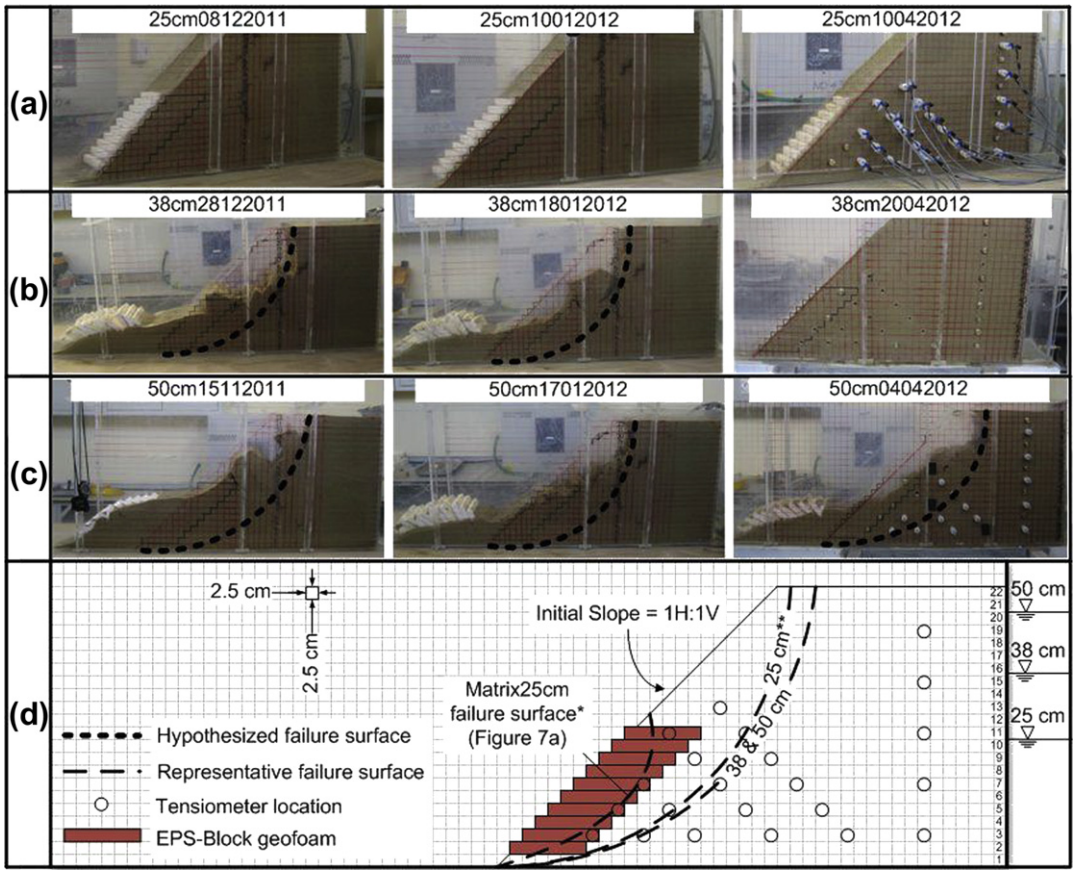

Fig. 16. Slope physical conditions and hypothesized failure surfaces at the end of the triplicate experiments of the "One Row Partial Bottom" configuration under (a) 25 cm-, (b) 38 cm-, and (c) 50 cm-H_2O pressure head boundary conditions. (d) Representative failure surfaces for each boundary condition.

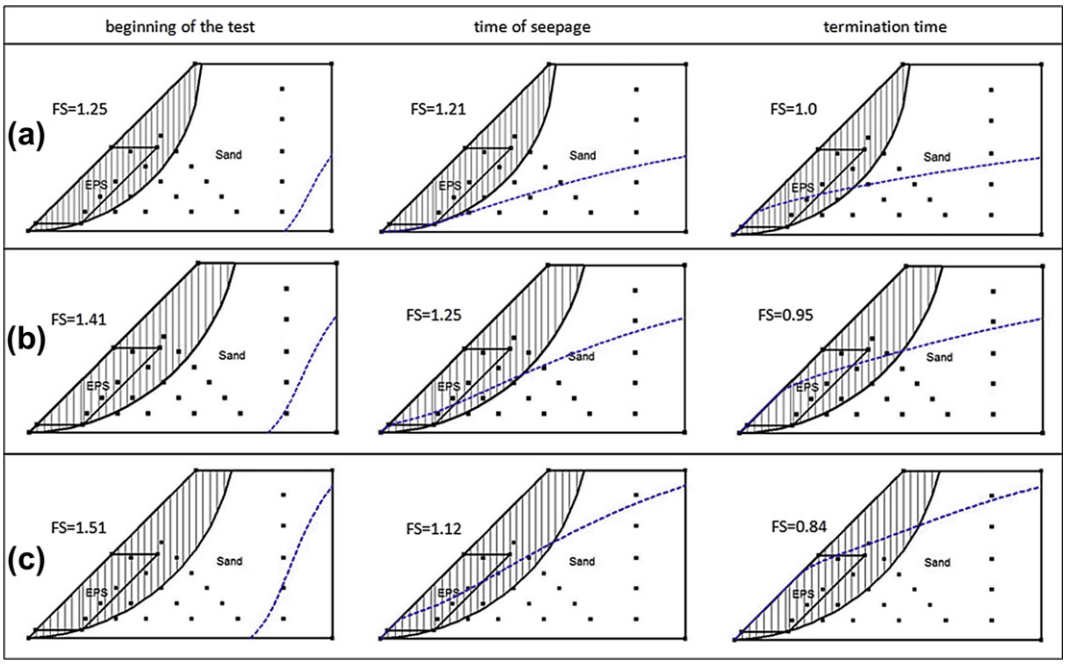

Fig. 17. Factor of safety (FS) of the "One Row Partial Bottom" configuration and the location of the phreatic surface at three different time intervals under (a) 25 cm-, (b) 38 cm-, and (c) 50 cm-H_2O pressure head boundary conditions.

the "One Row Partial Bottom" configuration (Fig. 16d), it can be seen that the shallow-seated failure surface stayed within the geofoam blocks similar to the situation of the "One Row" configuration (Fig. 12d). Confirming the laboratory observations which showed no failure at the end of the triplicate experiments (Fig. 16a), SLOPE/W calculated FS >1.0 for this failure surface since the strength properties of geofoam block (Table 1) governs the calculation of the FS.

Since both laboratory lysimeters experiments (Fig. 16a) and SLOPE/W did not show a failure through EPS-block geofoam under 25 cm-H_2O pressure head boundary condition, a failure surface which is located immediately behind the geofoam blocks was selected (indicated as "25 cm**" in Fig. 16d). FS values were reported for this deep-seated failure surface in Fig. 17a. The change in FS with time during the experiment for this failure surface can be found in Fig. 11d. It can be seen that the FS value remained above 1.0 throughout the experiment (Figs. 11a and d) where steady-state conditions were established (Fig. 8d). In addition, having almost identical tensiometer readings at the toe of the slope (Tensiometer 20) for all configurations suggested that the effect of the geofoam blocks on the hydrodynamics of the back-slope seepage flow was negligible. Therefore, during the numerical modeling of the seepage flow by SEEP/W, the hydraulic parameters of the back-slope soil were used for the geofoam blocks. The pore-water pressures calculated by SEEP/W were then used by SLOPE/W for the calculation of FS.

The FS calculated for the representative failure surface under 38 cm-H_2O pressure head boundary condition decreased from 1.41 (at initial condition) to 0.95 at the end of the experiment (Fig. 17b), which demonstrates a marginally stable condition (FS $\approx$1). This situation was also observed during the triplicate experiments by the failure of the two slopes (experiments: 38 cm28122011 and 38 cm18012012) and no failure of the third experiment (38 cm20042012). The change in FS during the experiment can be found in Fig. 11d.

Similar to "Matrix", "One Row", and "One Row Partial Top" configurations, the failure surface for the 50 cm-H_2O pressure head boundary condition was also deep-seated as shown by the hypothesized failure surfaces given in Fig. 16c. The FS values calculated by SLOPE/W for the representative failure surface given in Fig. 16d at the end of the experiments was 0.84 (Fig. 17c), and the variation of FS during the experiment can be found in Fig. 11d.

The hypothesis of using the hydraulic properties of sand for the geofoam block domain in the numerical models can be considered as valid, since the steady-state readings at the toe section of the slope (Tensiometer 20 in Fig. 8) recorded during laboratory tests remained unchanged (approximately around 8 cm-H_2O pressure head) for all configurations. This suggests that geofoam block system does not restrict groundwater flow within the back-slope and does not cause a pore-water pressure build-up as it would be the case if geofoam block system had a lower saturated hydraulic conductivity than that of sand.

4. Summary and conclusions

Considering all the failure surfaces obtained from the lysimeter experiments, it is important to note that none passed through the geofoam blocks due to their relatively high cohesive strength. Numerical models also confirmed this observation by computing relatively high factors of safety (FS >1.0) for the failure surfaces completely enclosed by geofoam blocks. All failure slope surfaces observed at the end of the lysimeter experiments were due to the global stability involving a "deep-seated" slip surface except for the shallow-seated failures which occurred in "Matrix" and "One Row Partial Top" configurations for the 25 cm-H_2O pressure head boundary condition. In addition, no floatation (uplift and sliding) of geofoam blocks was observed during the experiments. As a result, the prevailing behavior of the steep marginal stable sandy slope investigated in this study was controlled by the strength properties of the back-slope material and the pore-water pressure build-up resulting from the seepage behind the geofoam block configuration.

Thus it was concluded that geofoam block slope systems are a viable alternative remediation technique for shallow-seated failures under seepage in which the failed mass of the existing slope material could be replaced entirely with geofoam blocks. This may have a practical application at locations where spatial constraints do not permit slope flattening and land uses below the toe of the slope do not pose a significant risk to human life or property should the geofoam block remedial measures not perform as well as intended. However, the configurations tested in this study seemed to be ineffective to prevent "deep-seated" failures of a marginally stable steep slope. For "deep-seated" failures, it may not be feasible to replace the entire failed mass with geofoam blocks. This is due to the fact that the "deep-seated" failure surfaces tend to propagate towards the back-slope once the failed mass has been replaced by geofoam blocks.

For future work, we recommend that additional configurations of geofoam block not only be tested in the laboratory using 1-g small scale laboratory physical model test, but also be tested in the field by using fully instrumented prototype models in order to develop preventive strategies for "deep-seated" slope failures. In addition, it may be useful to investigate the possible interlocking effect of geofoam blocks in configurations where more than one stack of blocks are placed in a manner where vertical and horizontal joints are not continuous. In addition, more elaborate numerical modeling techniques will be required for complex failures that involve both shearing and sliding of the geofoam blocks that are part of a complex failure surface.

Based on the results of this study, it appears that a geofoam block system can be implemented for the remediation of seepage undercutting problems occurring in layered streambanks where shallow-seated failures cause significant soil loss provided that flotation (i.e., buoyancy uplift and block sliding) of geofoam blocks is not a concern, or where such a mechanism can be guarded against using other engineering countermeasures. In addition, geofoam block might be applied to remediate shallow-seated slope failures occurring due to seepage at the toe of an embankment, cut slope, and levees.

Acknowledgments

The laboratory experiments were conducted at Civil Engineering Laboratory at Okan University. The writers acknowledge the contributions of Halis Şahin, laboratory technician, and lysimeter packing team formed by undergraduate student assistants: Gönüllü Oğuz Şimşek, Anıl Çağatay, Aysun Sinan, Senem Özdemir, and Mehmet Oğuz.

References

Aabøe, R., 2011. 40 years of experience with the use of EPS geofoam blocks in road construction. In: Proceedings of 4th International Conference on Geofoam Blocks in Construction Applications, Lillestrøm, Norway.

Akay, O., Fox, G.A., 2007. Experimental investigation of direct connectivity between macropores and subsurface drains during infiltration. Soil Science Society of America Journal 71 (5), 1600–1606.

Akay, O., Fox, G.A., Šimůnek, J., 2008. Numerical simulation of flow dynamics during macropore–subsurface drain interactions using HYDRUS. Vadose Zone Journal 7 (3), 909–918.

Arellano, D., Stark, T.D., Horvath, J.S., Leshchinsky, D., 2009. Guidelines for Geofoam Applications in Slope Stability Projects: Interim Report. NCHRP Project 24-11(02). Transportation Research Board, Washington D.C., USA.
Arellano, D., Tatum, J.B., Stark, T.D., Horvath, J.S., Leshchinsky, D., 2010. A framework for the design guideline for EPS-block geofoam in slope stabilization and repair. Transportation Research Record 2170, 100–108.
Arellano, D., Stark, T.D., Horvath, J.S., Leshchinsky, D., 2011a. Guidelines for Geofoam Applications in Slope Stability Projects: Final Report. NCHRP Project No. 24-11(02). Transportation Research Board, Washington, D.C., USA. http://onlinepubs.trb.org/onlinepubs/nchrp/docs/NCHRP24-11(02)_FR.pdf.
Arellano, D., Stark, T.D., Horvath, J.S., Leshchinsky, D., Kafash, M.H., Wang, C., 2011b. Overview of NCHRP design guideline for EPS-block geofoam in slope stabilization and repair. In: Proceeding of 4th International Conference on Geofoam Blocks in Construction Applications, Lillestrøm, Norway.
Baram, S., Kurtzman, D., Dahan, O., 2012. Water percolation through a clayey vadose zone. Journal of Hydrology 424, 165–171.
Bartlett, S., Negussey, D., Kimble, M., Sheeley, M., 2000. Use of geofoam as superlightweight fill for I-15 reconstruction. In: Proceedings of Transportation Research Board 79th Annual Meeting, Washington, D.C., USA.
Bartlett, S.F., Farnsworth, C., Negussey, D., Stuedlein, A.W., 2001. Instrumentation and long-term monitoring of geofoam embankments, I-15 reconstruction project, Salt Lake City, Utah. In: Proceedings of the 3rd International EPS Geofoam Conference, Salt Lake City, Utah, USA.
Bartlett, S.F., Lingwall, B.N., Trandafir, A.C., Lawton, E.C., 2011. Protection of steel pipelines from permanent ground deformation using EPS geofoam. In: McDonough, P.W. (Ed.), Seismic Resilience of Natural Gas Systems – Improving Performance. Technical Council on Lifeline Earthquake Engineering Monograph, vol. 34. ASCE, Virginia, pp. 5–27.
Bathurst, R.J., Zarnani, S., Gaskin, A., 2007. Shaking table testing of geofoam seismic buffers. Soil Dynamics and Earthquake Engineering 27, 324–332.
Beinbrech, G., Hillmann, R., 1997. EPS in road construction – current situation in Germany. Geotextiles and Geomembranes 15, 39–57.
Ching-Chuan, H., Yih-Jang, J., Lih-Kang, H., Jin-Long, L., 2009. Internal soil moisture and piezometric responses to rainfall-induced shallow slope failures. Journal of Hydrology 370, 39–51.
Choudhary, A.K., Jha, J.N., Gill, K.S., 2010. Laboratory investigation of bearing capacity behavior of strip footing on reinforced flyash slope. Geotextiles and Geomembranes 28, 393–402.
Chu-Agor, M.L., Fox, G.A., Cancienne, R., Wilson, G.V., 2008. Seepage caused tension failures and erosion undercutting of hillslopes. Journal of Hydrology 359, 247–259.
Coulter, T.S., 1975. Woodwaste as lightweight fill in highway construction. In: Proceedings of 28th Conference of Western Association of Canadian Highway Officials, Winnepeg, British Columbia, Canada.
Dash, S.K., Sireesh, S., Sitharam, T.G., 2003. Model studies on circular footing supported on geocell reinforced sand underlain by soft clay. Geotextiles and Geomembranes 21, 197–219.
Duncan, J.M., Wright, S.G., 1980. The accuracy of equilibrium methods of slope stability analysis. In: Proceedings of International Symposium on Landslides, New Delhi, India.
Duskov, M., 1997. Materials research on EPS20 and EPS15 under representative conditions in pavement structures. Geotextiles and Geomembranes 15, 147–181.
EDO., 1996. In: Proceedings of International Symposium on EPS Construction Method (EPS Tokyo '96), Tokyo, Japan.
El Sawwaf, M.A., 2007. Behavior of strip footing on geogrid-reinforced sand over a soft clay slope. Geotextiles and Geomembranes 25, 50–60.
Elragi, A.F., 2000. Selected engineering properties and applications of EPS geofoam, Ph.D. Dissertation, State University of New York College of Environmental Science and Forestry, Syracuse, NY.
Farnsworth, C.B., Bartlett, S.F., Negussey, D., Stuedlein, A.W., 2008. Rapid construction and settlement behavior of embankment systems on soft foundation soils. Journal of Geotechnical and Geoenvironmental Engineering 134 (3), 289–301.
Fox, G.A., Wilson, G.V., 2010. The role of subsurface flow in hillslope and stream bank erosion: a review. Soil Science Society of America Journal 74 (3), 717–733.
Fox, G.A., Wilson, G.V., Periketi, R.K., Cullum, R.F., 2006. Sediment transport model for seepage erosion of streambank sediment. Journal of Hydrologic Engineering 11 (6), 603–611.
Fox, G.A., Wilson, G.V., Simon, A., Langendoen, E., Akay, O., Fuchs, J.W., 2007. Measuring streambank erosion due to ground water seepage: correlation to bank pore water pressure, precipitation and stream stage. Earth Surface Processes and Landforms 32, 1558–1573.
Geo-Slope International Ltd., 2008. Stability Modeling with SLOPE/W 2007, an Engineering Methodology, fourth ed.. Calgary, Alberta, Canada.
Geo-Slope International Ltd., 2009. Seepage Modeling with SEEP/W 2007, an Engineering Methodology, fourth ed.. Calgary, Alberta, Canada.
Horvath, J.S., 1997. The compressible inclusion function of EPS geofoam. Geotextiles and Geomembranes 15, 77–120.
Jia, G.W., Zhan, T.L.T., Chen, Y.M., Fredlund, D.G., 2009. Performance of a large-scale slope model subjected to rising and lowering water levels. Engineering Geology 106, 92–103.
Jutkofsky, W.S., Sung, J.T., Negussey, D., 2000. Stabilization of an embankment slope with geofoam. Journal of the Transportation Research Board 1736, 94–102.
Jutkofsky, W.S., 1998. Geofoam Stabilization of an Embankment Slope, a Case Study of Route 23A in the Town of Jewett, Greene County. Geotechnical Engineering Bureau, New York State Department of Transportation, Albany, NY, USA.
Kilian, A.P., 1984. Use of sawdust in landslide correction and settlement control. In: Proceedings of 35th Annual Road Builders, pp. 35–48.
Kousik, D., Samadhiya, N.K., Namdeo, J.B., 2011. Laboratory model studies on unreinforced and geogrid-reinforced sand bed over stone column-improved soft clay. Geotextiles and Geomembranes 29, 190–196.
Krahn, J., 2003. The 2001 R.M. Hardy Lecture: the limits of limit equilibrium analyses. Canadian Geotechnical Journal 40 (3), 643–660.
Latha, M.L., Somwanshi, A., 2009. Bearing capacity of square footings on geosynthetic reinforced sand. Geotextiles and Geomembranes 27, 281–294.
Lee, L.M., Kassim, A., Gofar, N., 2011. Performances of two instrumented laboratory models for the study of rainfall infiltration into unsaturated soils. Engineering Geology 117, 78–89.
Leshchinsky, D., Lambert, G., 1991. Failure of cohesionless model slopes reinforced with flexible and extensible inclusions. Transportation Research Record 1330, 54–63.
Lingwall, B., 2011. Development of an expanded polystyrene cover system for pipelines at fault crossings. Ph.D. Dissertation, Department of Civil and Environmental Engineering, University of Utah.
Lourenço, S.D.N., Sassa, K., Fukuoka, H., 2006. Failure process and hydrologic response of a two layer physical model: Implications for rainfall-induced landslides. Geomorphology 73, 115–130.
Mann, G., Stark, T.D., 2007. Slope stabilization using geofoam. In: Proceedings of Geo-Denver 2007: New Peaks in Geotechnics, GSP 161 Embankments, Dams, and Slopes. ASCE.
McKay, L.D., Cherry, J.A., Gillham, R.W., 1993. Field experiments in a fractured clay till .1. Hydraulic conductivity and fracture aperture. Water Resources Research 29 (4), 1149–1162.
Morgenstern, N.R., Price, V.E., 1967. The analysis of the stability of embankments assuming parallel interslice forces. Geotechnique 17, 11–26.
Moriasi, D.N., Arnold, J.G., Van Liew, M.W., Bingner, R.L., Harmel, R.D., Veith, T.L., 2007. Model evaluation guidelines for systematic quantification of accuracy in watershed simulations. Transactions of the ASABE 50 (3), 885–900.
Murillo, C., Thorel, L., Caicedo, B., 2009. Ground vibration isolation with geofoam barriers: centrifuge modeling. Geotextiles and Geomembranes 27, 423–434.
Negussey, D., Sun, M., 1996. Reducing lateral earth pressure by geofoam (EPS) substitution. In: Proceedings of the 2nd International Symposium on EPS Construction Method, Tokyo, Japan.
Negussey, D., 2002. Slope Stabilization with Geofoam. FHWA Research Project No. 2398P62000015. Geofoam Research Center, Syracuse University, Syracuse.
O'Brian, A.S., 2001. Design and construction of the UK's first polysterene embankment for railway use. In: Proceedings of the 3rd International EPS Geofoam Conference, Salt Lake City, Utah.
Ossa, A., Romo, M.P., 2010. Dynamic characterization of EPS geofoam. Geotextiles and Geomembranes 29, 40–50.
Prikryl, W., Williammee, R., Winter, M.G., 2005. Slope failure repair using tyre bales at interstate highway 30, Tarrant county, Texas, USA. Quarterly Journal of Engineering Geology and Hydrogeology 38, 377–386.
Read, J., Dodson, T., Thomas, J., 1991. Experimental Project Use of Shredded Tires for Lightweight Fill. Post-construction Report. Oregon Department of Transportation, Salem, Oregon.
Reuter, G., Rutz, J., 2000. A lightweight solution for landslide stabilization. Geotechnical Fabrics Report 18 (7), 42–43.
Reuter, G.R., 2001. Use of geofoam for landslide stabilization-CTH "A", Bayfield County, Wisconsin. In: Proceedings of the 3rd International Geofoam Conference, Salt Lake City, Utah.
Schnellmann, R., Busslinger, M., Schneider, H.R., Rahardjo, H., 2010. Effect of rising water table in an unsaturated slope. Engineering Geology 114, 71–83.
Sharma, S., Buu, T., 1992. Bud Peck slide, interstate 15 near Malad, Idaho. Journal of the Transportation Research Board 1343, 123–129.
Sheeley, M., 2000. Slope stabilization utilizing geofoam. M.S. Thesis, Syracuse University, Syracuse, N.Y.
Shipitalo, M.J., Nuutinen, V., Butt, K.R., 2004. Interaction of earthworm burrows and cracks in a clayey, subsurface-drained, soil. Applied Soil Ecology 26 (3), 209–217.
Šimůnek, J., van Genuchten, M.Th., 1996. Estimating unsaturated soil hydraulic properties from tension disc infiltrometer data by numerical inversion. Water Resources Research 32 (9), 2683–2696.
Šimůnek, J., van Genuchten, M.Th., 1997. Estimating unsaturated soil hydraulic properties from multiple tension disc infiltrometer data. Soil Science 162 (6), 383–398.
Šimůnek, J., van Genuchten, M.Th., Šejna, M., 2012. The HYDRUS Software Package for Simulating Two- and Three Dimensional Movement of Water, Heat, and Multiple Solutes in Variably-saturated Media, Technical Manual, Version 2.0. PC Progress, Prague, Czech Republic.
Spencer, E., 1967. A method of analysis of embankments assuming parallel inter slice forces. Geotechnique 17 (1), 11–26.
Stark, T.D., Arellano, D., Horvath, J.S., Leshchinsky, D., 2004a. Geofoam Applications in the Design and Construction of Highway Embankments. NCHRP Web Document 65 (Project 24-11). Transportation Research Board, Washington, D.C. http://trb.org/publications/nchrp/nchrp_w65.pdf.
Stark, T.D., Arellano, D., Horvath, J.S., Leshchinsky, D., 2004b. Guideline and Recommended Standard for Geofoam Applications in Highway Embankments. NCHRP Report 529. Transportation Research Board, Washington, D.C. http://trb.org/publications/nchrp/nchrp_rpt_529.pdf.

Trandafir, A.C., Bartlett, S.F., Lingwall, B.N., 2010. Behavior of EPS geofoam in stress-controlled cyclic uniaxial tests. Geotextiles and Geomembranes 28, 514–524.
Tsukamoto, H., 1996. Slope stabilization by the EPS method and its applications. In: Proceedings of the International Symposium on EPS Construction Method (EPS Tokyo '96), Tokyo, Japan.
van Genuchten, M.Th., Leij, F.J., Yates, S.R., 1991. The RETC Code for Quantifying the Hydraulic Functions of Unsaturated Soils, Version 1.0, EPA Report 600/2-91/065. U.S. Salinity Laboratory, USDA, ARS, Riverside, California.
van Genuchten, M.Th., 1980. A closed-form equation for predicting the hydraulicconductivity of unsaturated soils. Soil Science Society of America Journal 44 (5), 892–898.
Villholth, K.G., Jensen, K.H., Fredericia, J., 1998. Flow and transport processes in a macroporous subsurface-drained glacial till soil – I: field investigations. Journal of Hydrology 207 (1–2), 98–120.
Wilson, G.V., Periketi, R.K., Fox, G.A., Dabney, S.M., Shields, F.D., Cullum, R.F., 2007. Soil properties controlling seepage erosion contributions to streambank failure. Earth Surface Processes and Landforms 32, 447–459.
Wright, S.G., 1969. A study of slope stability and the undrained shear strength of clay shales. Ph.D. Dissertation, University of California, Berkley, CA.
Yan, Z.L., Wang, J.J., Chai, H.J., 2010. Influence of water level fluctuation on phreatic line in silty soil model slope. Engineering Geology 113, 90–98.
Yeh, S.T., Gilmore, J.B., 1989. Application of EPS for Slide Correction. In: Proceedings of Stability and Performance of Slopes and Embankments II, Berkeley, California.
Yoo, C., 2001. Laboratory investigation of bearing capacity behavior of strip footing on geogrid-reinforced sand slope. Geotextiles and Geomembranes 19, 279–298.
Zarnani, S., Bathurst, R.J., 2007. Experimental investigation of EPS geofoam seismic buffers using shaking table tests. Geosynthetics International 14 (3), 165–177.
Zimmerman, R.W., Bodvarsson, G.S., 1996. Hydraulic conductivity of rock fractures. Transport in Porous Media 23 (1), 1–30.